TECHNISCHE UNIVERSITÄT WIEN
Vienna University of Technology

Distributed Stray Field Calculation Using the Fast Multipole Method

DISSERTATION

zur Erlangung des akademischen Grades

Doktor der technischen Wissenschaften

eingereicht von

Dipl.-Ing. Pietro Palmesi

Matrikelnummer 00625876

an der

Fakultät für Festkörperphysik der Technischen Universität Wien

Betreuung: Assoz. Prof. Dipl.-Ing. Dr. Dieter Suess

Die Dissertation wurde begutachtet von:

(Assoz. Prof. Dipl.-Ing. Dr. Dieter Suess)	(Prof. Dr. Claudio Serpico)	(Assoz. Prof. Dr. Massimiliano d'Aquino)

Wien, 19. April 2018

(Dipl.-Ing. Pietro Palmesi)

TECHNISCHE
UNIVERSITÄT
WIEN
Vienna University of Technology

Distributed Stray Field Calculation Using the Fast Multipole Method

DISSERTATION

submitted in partial fulfillment of the requirements for the degree of

Doktor der technischen Wissenschaften

submitted by

Dipl.-Ing. Pietro Palmesi

Registration Number 00625876

to the
Faculty of Solid State Physics at the Vienna University of Technology
Advisor: Assoz. Prof. Dipl.-Ing. Dr. Dieter Suess

The dissertation has been reviewed by:

_____   _____   _____
(Assoz. Prof. Dipl.-Ing. Dr.   (Prof. Dr. Claudio Serpico)   (Assoz. Prof. Dr.
Dieter Suess)   Massimiliano d'Aquino)

Vienna, April 19, 2018   _____
                                                                                       (Dipl.-Ing. Pietro Palmesi)

Erklärung zur Verfassung der Arbeit

Dipl.-Ing. Pietro Palmesi
Hintzerstr. 2/18, 1030 Wien

Hiermit erkläre ich, dass ich diese Arbeit selbständig verfasst habe, dass ich die verwendeten Quellen und Hilfsmittel vollständig angegeben habe und dass ich die Stellen der Arbeit — einschließlich Tabellen, Karten und Abbildungen —, die anderen Werken oder dem Internet im Wortlaut oder dem Sinn nach entnommen sind, auf jeden Fall unter Angabe der Quelle als Entlehnung kenntlich gemacht habe.

_____

(Ort, Datum)

_____

(Unterschrift Dipl.-Ing. Pietro Palmesi)

Abstract

The long-range magnetic field is the most time-consuming part of micromagnetic simulations. Computational improvements can relieve problems related to this bottleneck. This work presents an efficient implementation of the Fast Multipole Method [FMM] for the magnetic scalar potential and stray field as used in micromagnetics. The novelty lies in extending FMM to linearly magnetized tetrahedral sources making it interesting also for other areas of computational physics. The near field is calculated directly, and the far field is approximated numerically using multipole expansion. This approach tackles important issues like the vectorial and continuous nature of the magnetic field. By using FMM the calculations scale linearly in time and memory and are distributed among many processors.

Kurzfassung

Das langreichweitige Streufeld ist der zeitaufwändigste Teil mikromagnetischer Simulationen. Durch die Verwendung des vorgestellten Algorithmus können damit verbundene Herausforderungen, wie Parallelisierung und asymptotische Zeitkomplexität, gelöst werden. Diese Arbeit stellt eine effiziente Umsetzung der Fast Multipole Method [FMM] für das magnetische Skalarpotential und Streufeld im Rahmen des Mikromagnetismus dar. Die Neuheit besteht darin, einen der vielversprechendsten Algorithmen unserer Zeit, nämlich FMM, auf linear magnetisierte tetraedrische Quellen auszudehnen und damit für mikromagnetische Probleme und potentiell auch für andere Bereiche der computergestützten Physik interessant zu machen. Die hier vorgestellte Implementierung berechnet das Nahfeld exakt. Das Fernfeld wird hingegen mittels numerischer Integration auf Basis der Multipolentwicklung approximiert. Diese Arbeit löst grundlegende Problemen der Implementierung, wie die Abbildung der vektoriellen und kontinuierlichen Natur des Magnetfeldes auf die ursprünglich nicht kontinuierliche FMM. Es wird gezeigt, dass die Berechnungen linear in Zeit und Speicher über viele Rechenkerne hinweg skalieren und dabei eine für mikromagnetische Standardprobleme ausreichende Genauigkeit erreichen.

Acknowledgements

To my wife Anna, for her love, support, and proof-reading this thesis.

My supportive father, who has always encouraged me: Grazie per avermi sempre sostenuto. Sei stato una stella fissa che mi ha dato il calore e la fiducia di cui ogni essere umano ha bisogno. My late mother for giving me a happy childhood and teaching me the value of knowledge and sensitivity.

I want to express my sincere gratitude to my advisor Dieter Suess for enabling this thesis and creating an atmosphere of trust, enthusiasm, and fun in our group. I also want to thank all the colleagues in our research group with a special mention to Claas Abert and Florian Bruckner for countless discussions and for giving directions on how to move forward. I further want to thank my best man and longtime friend Anton Bachleitner-Hofmann for sharing this long and exciting journey from preschool to postgraduate.

Contents

Contents

1. Introduction

Magnetism plays a vital role in everyday life. Not only in the form of the geo-magnetic field protecting us from solar winds and charged particles, but also in many technological applications like motors, hard disk drives, MRAM, sensors, and spintronics. For the improvement and development of new magnetic applications, a thorough theoretical understanding of magnetism is required. For many larger applications *ab initio* calculations are not feasible, and thus micromagnetic theory and simulations come into use.

Micromagnetism is a branch of magnetism operating in the micron region. It has been successfully used to model and develop hard drives by improving write heads and storage material [1, 2, 3]. Other applications include the development of magnetic random access memory [MRAM] [4, 5] and recent developments like racetrack memory [6]. Another use of micromagnetism is the investigation of hard magnetic materials [7].

The long-range magnetic stray field is a bottleneck for large micromagnetic simulations. This thesis presents a method for improving the scaling of simulations in time, memory and the parallelization to distributed systems by using the Fast Multipole Method and extending it to continuous sources.

This thesis comprises seven sections starting with this introduction. Chapter 2 explains the basic tenants of magnetism and introduces and describes relevant variables. The magnetic concepts are refined in chapter 3 explaining applicability and basic concepts of micromagnetism. Chapter 4 is the theoretical centerpiece of the thesis describing the Fast Multipole Method and its adaption for the continuous micromagnetic demagnetizing field. Chapter 5 provides an excerpt of the

documentation generated from the implementation. The simulation results are presented and discussed in chapter 6. Chapter 7 is the last section; it addresses shortcomings of the method and potential improvements.

2. Magnetism

2.1. Overview of Magnetic Theories

To describe and calculate the whole size spectrum of magnetic materials magnetic models can be divided into five overlapping models (see table 2.1).

Table 2.1.: This table gives a hierarchy of common magnetic theories their domains of application, a short explanation, and approximate dimensional applicability.

Name	Description	Order of magnitude
Atomistic theory	QM ab initio	less than $1\,\mathrm{nm}$
Micromagnetic theory	Domain wall structure	$1\,\mathrm{nm}$ to $1000\,\mathrm{nm}$
Domain theory	Microstructure of domains	$1\,\mathrm{\mu m}$ to $1000\,\mathrm{\mu m}$
Maxwell solvers	Macroscopic description	more than $0.01\,\mathrm{mm}$
Phase theory	Ensemble description	more than $0.1\,\mathrm{mm}$
Magnetic Hysteresis		Always applicable

The most fundamental ab initio theories are using charges and spins in a quantum mechanical model to describe the magnetic properties of magnetic materials. Only the most basic systems can be calculated without severe approximations [8]. On top of that ab initio based theories scale poorly to larger systems ($\mathcal{O}(\exp(N))$).

The micromagnetic theory is a continuous semiclassical theory describing magnetic materials from a few nanometers to the order of microns which are much larger than ab initio calculations would allow. It can explain many magnetic effects like the formation of domain walls and their pinning in bulk material and thin films. It can be used to describe ferromagnetic materials such as nanocrystalline and
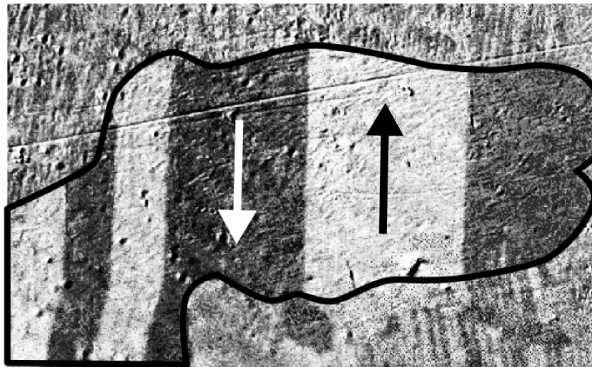
2. Magnetism

Figure 2.1.: Domain wall structure of a single grain outlined in black with an arrow pointing in the direction of the magnetization. *This image was created by Chris Vardon Zureks and is licensed under the Creative Commons Attribution-Share Alike 3.0 Unported license.*

amorphous alloys as well as intermetallic compounds [9]. In contrast to domain theory, it allows the resolution of domain wall structures.

Domain walls (see figure 2.1) are uniformly magnetized regions in otherwise heterogeneous magnetic structures [10]. They can be observed via magneto-optical methods. According to Becker and Döring [11] domain wall theory can accurately describe crystal anisotropy, displacement of domain walls, and the rotation of magnetization vectors inside the domains. Exchange interaction can be expressed by a term using the exchange constant in a similar way as in micromagnetism. Domain wall theory is a simpler, more macroscopic model than micromagnetism which can be used more efficiently on larger structures. On the other hand, it cannot describe the magnetic behavior of small particles without a regular domain structure, the domain wall structure itself, rapid dynamic magnetization reactions, and stability limits.

Macroscopic Maxwell Solvers [12] use the macroscopic Maxwell equations to describe averaged magnetic regions. In practice, this means that the magnitude of the magnetization is not constant and the material properties get more complicated (i.e., non-linear). The time-saving factor of this method is that the discretization regions can be much larger compared to micromagnetic simulations. This method has successfully been coupled to the micromagnetic model by [13], effi-

20

ciently combining the applicability of both models for problems where the domain wall structure is only relevant in some parts of the geometry.

In phase theory only the phase volumes of domains with parallel magnetization are essential. The arrangement of the domains is irrelevant, which is true for, e.g., small high-anisotropy particles and large soft-magnetic structures. It provides a mostly shape-independent vectorial magnetization curve for large samples which should agree with the measured anhysteretic magnetization curve. It does not accurately describe interfacial effects.

The hysteresis is a description of the magnetization depending on the external field and its history. It usually plots the magnetization against the magnetic field. After applying a field, the magnetization remains magnetized with remanence magnetization and needs a so-called coercive field to become demagnetized. Various mathematical descriptions of the underlying phenomena can be found in the literature [14, 15, 16, 17, 18].

2.2. Important Magnetic Concepts and Variables

The sources of permanent magnetic moments in solids are unpaired electron spins obeying Hund's rules in the atomic shells [19]. The moments of the nuclei are orders of magnitude smaller, and their contribution is negligible compared to the atomic moment. The atomic moments are coupled via exchange interaction which can give rise to magnetic order below Curie temperature. The resulting magnetization creates a magnetic field. Both the magnetization and its magnetic field are dependent on an external field in a nonlinear and irreversible manner.

2.2.1. Magnetization

Magnets are physically described by their dipole moment $\boldsymbol{\mu}$. In 1820 Oersted [19] discovered that electric currents produce an equivalent field to magnets and defined

the magnetic moment in terms of a current loop with area $\mathbf{A}$ and current I to be

$$\boldsymbol{\mu} = I\mathbf{A}. \tag{2.1}$$

The dipole moment $\boldsymbol{\mu}$ of a magnet is the sum of its atomic dipole moments $\boldsymbol{\mu}_i$ and the magnetization $\mathbf{M}$ is the moment per unit volume. Two sources of magnetic moments were found in nature, the aforementioned current loops and the so-called spin which is a trait of elementary particles.

2.2.2. Magnetic Field

The *magnetic field* $\mathbf{H}$ is a vector field created by a magnet or a current. It has the same unit as the magnetization, namely $\mathrm{A\,m^{-1}}$. The magnetic field drives the magnetization inside of magnetic solids. The relationship between the magnetization $\mathbf{M}$ and the magnetic field $\mathbf{H}$ is nonlinear, multivariate, and depending on the current magnetization, the dimensions, and the shape of the magnetic solid. The curve characterizing the magnetization as a function of the magnetic field $\mathbf{M}(\mathbf{H})$ is called the hysteresis.

It should be noted that the field $\mathbf{H}$ inside a magnet consists of an external field $\mathbf{H}_{\mathrm{ext}}$, which exists in the absence of the magnet and an internal *demagnetizing field* $\mathbf{H}_{\mathrm{d}}$ caused by the magnet.

$$\mathbf{H} = \mathbf{H}_{\mathrm{ext}} + \mathbf{H}_{\mathrm{d}} \tag{2.2}$$

The demagnetizing field is called *stray field* when it works outside the magnet. It is a long-ranged field and the primary focus of this thesis. In a continuous approximation, it can be calculated from the magnetization as

$$\mathbf{H}_{\mathrm{d}}(\mathbf{r}) = -\frac{1}{4\pi} \int_{\Omega} \mathbf{M}(\mathbf{r}_t) \cdot \nabla_t \frac{1}{|\mathbf{r} - \mathbf{r}_t|} \, \mathrm{d}^3 \mathbf{r}_t. \tag{2.3}$$

More detail about the stray field is given in section 3.1.2.
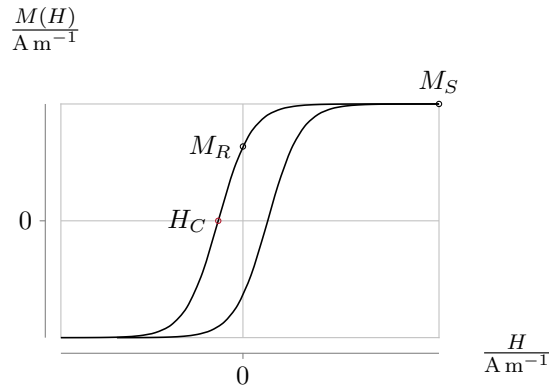
Figure 2.2.: Irreversible hysteresis loop with characteristic variables remanence magnetization M_R, saturation magnetization M_S, and coercive field H_C.

2.2.3. Hysteresis

> The hysteresis loop is the central datum of permanent magnetism; physicists want to understand it, material scientists want to improve it and engineers want to exploit it in useful applications.
>
> R. Skomski

The hysteresis loop usually plots the magnetization $\mathbf{M}$ against $\mathbf{H}$ as seen in figure 2.2. It shows how the magnetization responds to an external $\mathbf{H}$ field. Imagine a magnet in a large field. In figure 2.2, this is shown on the far right where the magnetization has reached its maximum, the so-called saturation magnetization M_S. By slowly reversing the field the magnetization changes along the upper curve. When the external field reaches zero, the remaining magnetization is called remanence magnetization M_R. Further reducing the field to the coercive field H_C, the magnetization reaches zero (i.e., the magnet displays no *remanent* magnetization). After reducing the field more, the magnetization reaches negative saturation on the far left. When the field is increased again, the magnetization behaves similarly as before, moving along the right curve in figure 2.2.

2.2.4. Magnetic Flux Density

The magnetic flux density **B** is closely related to the field **H**. In a vacuum, they are the same except for a constant $\mathbf{B} = \mu_0\mathbf{H}$. The constant $\mu_0 = 4\pi \times 10^{-7} Hm^{-1}$ is called vacuum permeability. In a magnet the flux density is given by

$$\mathbf{B} = \mu_0(\mathbf{M} + \mathbf{H}), \tag{2.4}$$

which means that magnetic field and flux density need not be parallel inside magnets. The magnetic flux density is solenoidal, i.e., its divergence is zero

$$\mathrm{div}\mathbf{B} = 0, \tag{2.5}$$

whereas the magnetic field is conservative, i.e., curl-free:

$$\mathrm{rot}\mathbf{H} = 0 \tag{2.6}$$

Conservative fields have the properties that line integrals are path-independent, that line integrals over closed loops are zero, and that the field **H** can be written as the gradient of a potential u:

$$\mathbf{H} = -\nabla u \tag{2.7}$$

The unit of the flux density is Tesla $[B] = T = [\mu_0]\mathrm{A\,m^{-1}}$, and some exemplary values are given in table 2.2. The magnetic flux density is one of two electromag-

Table 2.2.: Technical **B** values of various objects.

Object	Flux density **B**
Brain	$1\,\mathrm{nT}$
Earth magnetic field	$50\,\mathrm{mT}$
Pure iron	$2.15\,\mathrm{T}$
Super conducting magnets	$15\,\mathrm{T}$
Current pulse inside coil	$100\,\mathrm{T}$

netic variables exerting force on an electric charge. In 1865 James Clerk Maxwell

[20] already used the magnetic flux for describing the force $\mathbf{F}$ on an electric charge q as

$$\mathbf{F} = q(\mathbf{E} + \mathbf{vB}), \tag{2.8}$$

where $\mathbf{E}$ is the electric field.

2.2.5. Susceptibility

Above the Curie temperature T_C, the initial response of the magnetization $\mathbf{m}$ to an external field $\mathbf{H}$ is usually linear with the proportionality factor χ.

$$\mathbf{M} = \chi\mathbf{H} \tag{2.9}$$

The proportionality factor χ is called susceptibility. In many cases χ is a scalar, but it can be generalized to simple crystals by using χ as a matrix. For spin-paramagnetism, the temperature dependence of χ follows the Curie Law

$$\chi = \frac{C}{T}, \tag{2.10}$$

where C is a material dependent Curie constant.

For ferromagnets above the Curie temperature, the Curie-Weiss law has to be used instead:

$$\chi = \frac{C}{T - T_C} \tag{2.11}$$

The Curie-Weiss law predicts a singularity of χ at Curie temperature T_C below which the material is ferromagnetic.

For a ferromagnet, the susceptibility is usually generalized to

$$\chi = \frac{\partial\mathbf{M}}{\partial\mathbf{H}}. \tag{2.12}$$

2.2.6. Magnetic Anisotropy

Magnetic anisotropy describes the directional preference of magnetization relative to the crystal axes of the material in magnets. In contrast, isotropy describes directionally independent magnets where the energy of the system is independent of the crystal structure. In practice, ferromagnets are only isotropic in bulk materials where the microstructure features various directional components with a random distribution.

In the simplest case, the magnetization favors magnetization along a single axis, the *easy axis*. The source of the anisotropy is the crystal field. Uniaxial magnetic anisotropy is usually described using the anisotropy constant K_1 which expresses the anisotropy in terms of its energy contribution E_a:

$$E_a = -\int K_1 \cos^2(\theta) \, \mathrm{d}^3\mathbf{r} = -\int K_1 (\mathbf{M} \cdot \mathbf{e}_e)^2 \, \mathrm{d}^3\mathbf{r}, \qquad (2.13)$$

where θ is the angle between magnetization and easy axis $\mathbf{e}_e$. Typical anisotropy values are between $K_1 = 0.03 \, \mathrm{MJ\,m^{-3}}$ for hematite and $K_1 = 17.2 \, \mathrm{MJ\,m^{-3}}$ for $SmCo_5$.

For ellipsoidal shapes, the demagnetizing field can formally be treated as a so-called *shape anisotropy* of the ferromagnet (see section 3.1.2).

2.2.7. Magnetic Domain

A magnetic domain is a region with uniform magnetization in a ferromagnet [21]. Its parallelism arises from the exchange interaction, whereas the formation of domains stems from other interactions like the demagnetization field (see section 3.1.2) and grains with non-aligned anisotropies. Narrow *domain walls* separate the magnetic domains. The magnetization inside the domain walls can vary either in the plane of the domain wall (Bloch Wall) or perpendicular to the domain wall plane (Neél Wall).

3. Micromagnetism

The theory of magnetism is based on the work of Weiss, Landau and Lifshitz [22, 23] and was unified by Brown Jr [24] as the theory of *micromagnetism*.

Micromagnetism is a continuous description of ferromagnets with spontaneous magnetization below the Curie temperature T_C. Electrons with overlapping spin wave functions favor parallel alignment of elementary moments $\boldsymbol{\mu}_i$ at positions $\mathbf{r}_i$:

$$\boldsymbol{\mu}_i \approx \boldsymbol{\mu}_j \text{ for } |\mathbf{r}_i - \mathbf{r}_j| < \lambda, \tag{3.1}$$

which can be described by the exchange interaction (see section 3.1.1). λ is called the exchange length and is a measure of the range of the exchange interaction. With that the magnetic moments $\boldsymbol{\mu}_i$ inside a region Ω larger than λ^3 can be approximated by a continuous magnetization $\mathbf{M}(\mathbf{r})$:

$$\sum_i \boldsymbol{\mu}_i \approx \int_\Omega \mathbf{M}(\mathbf{r}) \, \mathrm{d}^3\mathbf{r}, \tag{3.2}$$

making the exchange length λ an important variable for the applicability of the micromagnetic theory.

For a uniform magnetization density $\mathbf{M}_i$, the magnitude of the magnetization $|\mathbf{M}(\mathbf{r})|$ can be assumed to be constant at the saturation magnetization M_S and the reduced magnetization $\mathbf{m}$:

$$\mathbf{M}(\mathbf{r}) = M_S \mathbf{m}(\mathbf{r}) \text{ with } |\mathbf{m}(\mathbf{r})| = 1 \tag{3.3}$$

27

The continuous magnetization is already used in classical electromagnetism, but for micromagnetism, additional non-classical effects like exchange interaction must be taken into account. These terms and their relevance for calculating the magnetization are explained in the next sections. The time evolution of the magnetization can be described by the Landau-Lifshitz-Gilbert equation which is described in section 3.2.

3.1. Energy Contributions in Micromagnetism

The local magnetization $\mathbf{M}(\mathbf{r})$ of a stable magnetization configuration and its dynamic behavior can be obtained by energy minimization of the total energy functional E_{tot}. The energy functional consists of many physical terms of classical and quantum mechanical origin

$$E_{\text{tot}} = E_{\text{ex}} + E_{\text{a}} + E_{\text{d}} + E_{\text{ext}} + \dots, \tag{3.4}$$

containing exchange energy E_{ex}, anisotropy energy E_{a}, and demagnetizing energy E_{d} described in the following sections as well as the Zeeman E_{ext} energy from the external field:

$$E_{\text{ext}} = - \int_{\Omega} \mu_0 \mathbf{M}(\mathbf{r}) \cdot \mathbf{H} V \, \mathrm{d}^3 \mathbf{r} \tag{3.5}$$

These competing energy terms, which are dependent on various external conditions, are responsible for the complex behavior of magnets.

3.1.1. Exchange Energy

Classical electrodynamics cannot explain magnetic order. According to classical electrodynamics, an ensemble of dipoles should have an anti-parallel order in its ground state [25]. Other magnetic materials like paramagnetic materials and diamagnetic materials avoid macroscopically parallel alignment as well.

An effect that aligns the magnetization in magnets is necessary for macroscopic magnetization to exist. This effect is called exchange interaction, and the related

energy is called exchange energy. Exchange interaction is a quantum mechanical effect with two contributions: a symmetric contribution postulated by Werner Heisenberg in 1926 [26, 27] and an antisymmetric Dzyaloshinskii-Moriya [28] term. The symmetric Hamiltonian $\mathcal{H}$ for the simplest case of two fermions with overlapping wave functions and spins $\mathbf{S}_i, \mathbf{S}_j$ without external field is

$$\mathcal{H} = -J \sum_{l,\delta} \mathbf{S}_l \mathbf{S}_{l+\delta}, \tag{3.6}$$

with the exchange integral J, describing the strength of the interaction and δ usually indicating next neighbors.

In classical terms, the Heisenberg operator becomes the energy and with the magnitude of the spins $S = |\mathbf{S}|$ and the unit vectors $\mathbf{n}_i = \mathbf{S}_i/S$ the energy for two spins reads:

$$E_{ij} = -J_{ij}S^2 \mathbf{n}_i \cdot \mathbf{n}_j \tag{3.7}$$

$$= -J_{ij}S^2 \left(1 - \frac{1}{2}(\mathbf{n}_i - \mathbf{n}_j)^2 \right) \tag{3.8}$$

The energy for the whole volume is the sum over all spins

$$E = \sum_{i,j} -J_{ij}S^2 \left(1 - \frac{1}{2}(\mathbf{n}_i - \mathbf{n}_j)^2 \right), \tag{3.9}$$

with the exchange integral J_{ij} describing the interaction between spins $\mathbf{S}_i$ and $\mathbf{S}_j$. Usually $J_{ij} \neq 0$ only for neighboring spins.

In the continuum, $\mathbf{n}_i \cdot \mathbf{n}_j$ becomes

$$\mathbf{m}(\mathbf{r}) \cdot \mathbf{m}(\mathbf{r} + \Delta\mathbf{r}) \approx 1 - \frac{1}{2}(\mathbf{m}(\mathbf{r}) - \mathbf{m}(\mathbf{r} + \Delta\mathbf{r}))^2, \tag{3.10}$$

with the lattice vector $\Delta\mathbf{r}$. Expansion around $\Delta\mathbf{r}$ gives

$$\mathbf{m}(\mathbf{r}) \cdot \mathbf{m}(\mathbf{r} + \Delta\mathbf{r}) \approx 1 - \frac{1}{2} \sum_i (\Delta\mathbf{r} \cdot m_i)^2, \tag{3.11}$$

with the three reduced magnetization components m_i. The energy for a general (i.e., not isotropic or cubic) material is

$$E = M_S^2 \int_\Omega \sum_{i,j,k} A_{ij} \frac{\partial m_i}{\partial x_j} \frac{\partial m_i}{\partial x_k} \, \mathrm{d}^3 x \tag{3.12}$$

which in the isotropic case simplifies to [21]

$$E = M_S^2 \int_\Omega A(\nabla \mathbf{m})^2 \, \mathrm{d}^3 \mathbf{r} = \int_\Omega A(\nabla m_x)^2 + (\nabla m_y)^2 + (\nabla m_z)^2 \, \mathrm{d}^3 \mathbf{r}. \tag{3.13}$$

Equation (3.13) can be interpreted as an energy that is zero when the magnetization is aligned uniformly and grows when the angle between nearby magnetization values change. The antisymmetric Dzyaloshinskii-Moriya interaction [DMI] is not treated in this thesis. A proper description can be found in [28, 29, 21].

3.1.2. Stray-Field Energy and Potential

The stray-field energy E_D is also known as magnetostatic or dipolar energy. It is called demagnetizing field, because it points opposite the magnetization inside the magnet, effectively reducing the field inside the magnet. It is similar to the external Zeeman energy, but caused by the magnet's own demagnetizing field $\mathbf{H}_D$ instead of the external field:

$$E_D = -\frac{\mu_0}{2} \int \mathbf{M} \cdot \mathbf{H}_D \, \mathrm{d}^3 \mathbf{r} \tag{3.14}$$

The demagnetization energy can be derived from Maxwell's equations and the conservation of energy [30], the factor of $\frac{1}{2}$ arises from the fact that the self-interaction should not be counted twice (once for $\mathbf{M}(\mathbf{r})$ and once for $\mathbf{M}(\mathbf{r}')$) when integrating over it. The electrostatic equations without currents

$$\mathrm{div}\mathbf{B} = 0 \tag{3.15}$$

$$\mathrm{rot}\mathbf{H}_D = 0 \tag{3.16}$$

allow the field $\mathbf{H}_D$ to be written as the gradient of the magnetic scalar potential u

$$\mathbf{H}_D = -\nabla u \tag{3.17}$$

and with equation (3.15)

$$\Delta u = \mathrm{div}\mathbf{M} = -\mathrm{div}\mathbf{H}_D. \tag{3.18}$$

The potential $u(\mathbf{r})$ has gauge invariance under transformations $u(\mathbf{r}) \to u(\mathbf{r}) + C$ and can be arbitrarily fixed asymptotically to

$$u(\mathbf{r}) = \mathcal{O}\left(\frac{1}{\mathbf{r}}\right) \quad \text{for } |\mathbf{r}| \to \infty, \tag{3.19}$$

usually referred to as open boundary condition. With the Greens function $\frac{1}{|\mathbf{r}-\mathbf{r}'|}$ of the Poisson function (3.18), the potential can be computed [25] as

$$u(\mathbf{r}) = -\frac{1}{4\pi} \int_\Omega \mathbf{M}(\mathbf{r}_s) \cdot \nabla_s \frac{1}{|\mathbf{r} - \mathbf{r}_s|} \, \mathrm{d}^3\mathbf{r}_s, \tag{3.20}$$

when the magnetization $\mathbf{M}(\mathbf{r}_s)$ is restricted to a source region $\mathbf{r}_s \in \Omega$.

The *conjunct* integral formulation (3.20) involves only one triple integral. By contrast, the *disjunct* formulation (3.21) uses a separate volume and surface integral:

$$u(\mathbf{r}) = \frac{1}{4\pi}\left[\int_\Omega \frac{\nabla_s \cdot \mathbf{M}(\mathbf{r}_s)}{|\mathbf{r} - \mathbf{r}_s|} \, \mathrm{d}^3\mathbf{r}_s - \int_{\partial\Omega} \frac{\mathbf{M}(\mathbf{r}_s) \cdot \mathbf{n}(\mathbf{r}_s)}{|\mathbf{r} - \mathbf{r}_s|} \, \mathrm{d}^2\mathbf{r}_s\right], \tag{3.21}$$

where $\mathbf{n}$ is the outward-pointing unit normal vector. The field $\mathbf{H}(\mathbf{r}_t)$ at the target point $\mathbf{r}_t$ can be easily computed by inserting equation (3.21) into equation (3.17):

$$\begin{aligned}
\mathbf{H}_D(\mathbf{r}_t) = -\frac{1}{4\pi}\Bigg[&\int_\Omega \nabla_s \cdot \mathbf{M}(\mathbf{r}_s)\nabla_t \frac{1}{|\mathbf{r}_t - \mathbf{r}_s|} \, \mathrm{d}^3\mathbf{r}_s \\
&- \int_{\partial\Omega} \mathbf{M}(\mathbf{r}_s) \cdot \mathbf{n}(\mathbf{r}_s)\nabla_t \frac{1}{|\mathbf{r}_t - \mathbf{r}_s|} \, \mathrm{d}^2\mathbf{r}_s\Bigg]
\end{aligned} \tag{3.22}$$

This thesis uses tetrahedral meshes and thus calculates the shape anisotropy directly by integrating equations (3.21) and (3.22), but for constantly-magnetized

ellipsoidal geometries equation (3.22) simplifies to

$$\mathbf{H}_D = -\lambda\mathbf{M}, \tag{3.23}$$

where λ is formally equal to an anisotropy and hence called *shape anisotropy*. Some λ for various geometries are given in table 3.1.

Table 3.1.: λ parameters for various ellipsoidal geometries

Geometry	λ
Sphere	$1/3$
Needle along its symmetry axis	0
Thin plate along its symmetry axis	1

3.1.3. Effective Field

The effective field

$$\mathbf{H}_{\mathrm{eff}} = \mathbf{H}_{\mathrm{ex}} + \mathbf{H}_{\mathrm{a}} + \mathbf{H}_{\mathrm{d}} + \mathbf{H}_{\mathrm{ext}} + \dots \tag{3.24}$$

is the field corresponding to the local contribution $e_{\mathrm{tot}}(\mathbf{r})$ of the total energy [31]

$$E_{\mathrm{tot}} = \int e_{\mathrm{tot}}(\mathbf{r})\,\mathrm{d}^3\mathbf{r}. \tag{3.25}$$

Some components like the external Zeeman field (equation (3.5)) or the demagnetization field can be measured directly. The Zeeman field is usually given or created, and the demagnetization field can be calculated by equation (3.22). Other contributions need to be calculated by the functional derivation of the respective energy contributions:

$$\mathbf{H}_{\mathrm{eff}}(\mathbf{r}) = -\frac{1}{\mu_0 M_S}\frac{\delta E_{\mathrm{tot}}}{\delta\mathbf{m}} \tag{3.26}$$

For the exchange energy (equation (3.13)) the field computes to

$$\mathbf{H}_{\mathrm{ex}}(\mathbf{r}) = -\frac{A}{\mu_0 M_S}\frac{\delta}{\delta\mathbf{m}}(\nabla\mathbf{m})^2 \tag{3.27}$$
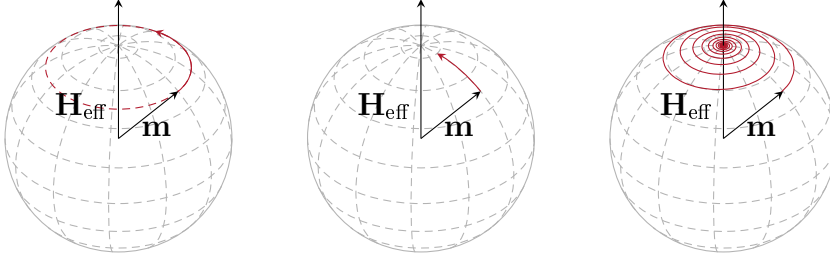
$$= \frac{2A}{\mu_0 M_S}\Delta\mathbf{m} \tag{3.28}$$

Figure 3.1.: Sketch of the LLG equation operating on a magnetic moment **m** via the effective field $\mathbf{H}_{eff}$. The left sphere shows the precessional term, the sphere in the center the damping term, and the figure on the right shows the superposition of both terms.

and for a uniaxial anisotropy from equation (2.13):

$$\frac{\delta E_a}{\delta \mathbf{m}} = -\frac{2K_1}{\mu_0 M_S}\mathbf{e}_e(\mathbf{e}_e \cdot \mathbf{m}) \tag{3.29}$$

3.2. LLG Equation

The Landau-Lifshitz-Gilbert [LLG] equation describes the time-dependent magnetization dynamics in micromagnetism. An earlier version was proposed by Landau and Lifshitz [23] in 1935. This chapter is based on the excellent description in [32]. The LLG equation

$$\partial_t \mathbf{m} = \underbrace{-\gamma(\mathbf{m} \times \mathbf{H}_{\text{eff}})}_{\text{precession}} + \underbrace{\alpha(\mathbf{m} \times \partial_t \mathbf{m})}_{\text{damping}} \tag{3.30}$$

consists of a precessional term stemming from spin dynamics and a phenomenological damping term (see figure 3.1). The damping term was historically seen as a relativistic effect, but a more contemporary interpretation deems it a dissipative effect similar to friction. The damping term was improved 1955 by Gilbert [33, 34] using a Lagrangian approach (see section 3.2.1). In the following sections two methods for deriving the LLG equation are presented, namely a Lagrangian and a quantum mechanical approach. The LLG equation contains a time derivative; thus an initial value $\mathbf{m}(\mathbf{r}, t = 0)$ has to be fixed to calculate the time evolution.

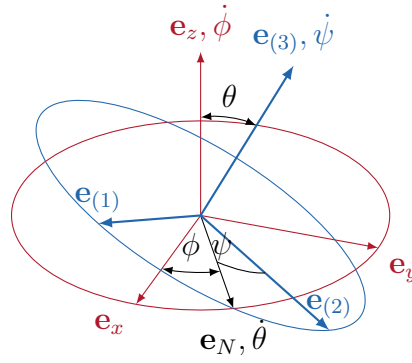Figure 3.2.: Euler angles ϕ, θ, and ψ describe the tranformation from one coordinate system $\mathbf{e}_x, \mathbf{e}_y, \mathbf{e}_z$ to a rotated coordinate system $\mathbf{e}_{(1)}, \mathbf{e}_{(2)}, \mathbf{e}_{(3)}$. The three vectors $\dot{\phi}, \dot{\theta}$, and $\dot{\psi}$ describe the constituents of the angular velocity around their respective axes.

3.2.1. Lagrangian Approach

To deduce the Lagrangian equation of motion, the reduced magnetic moment $\mathbf{m}(\mathbf{r})$ is described by Euler angles $\theta(\mathbf{r}), \phi(\mathbf{r})$, and $\psi(\mathbf{r})$ (see figure 3.2). For readability the local dependence of $\mathbf{r}$ is omitted in the following section.

The node vector $\mathbf{e}_N$ and anti-node vector $\mathbf{e}_A$ are used to describe the tilted rotation axis of $\mathbf{m}$:

$$\mathbf{e}_N = \mathbf{e}_x \sin\theta \sin\phi - \mathbf{e}_y \sin\theta \cos\phi + \mathbf{e}_z \cos\theta \tag{3.31}$$

$$\mathbf{e}_A = -\mathbf{e}_x \cos\theta \sin\phi + \mathbf{e}_y \cos\theta \cos\phi + \mathbf{e}_z \sin\theta \tag{3.32}$$

The tilted basis vectors can be written as

$$\mathbf{e}_{(1)} = \cos\psi \mathbf{e}_N + \sin\psi \mathbf{e}_A, \tag{3.33}$$

$$\mathbf{e}_{(2)} = -\sin\psi \mathbf{e}_N + \cos\psi \mathbf{e}_A, \tag{3.34}$$

and

$$\mathbf{e}_{(3)} = \sin\theta \cos\phi \mathbf{e}_x - \sin\theta \cos\phi \mathbf{e}_y + \cos\theta \mathbf{e}_z, \tag{3.35}$$

using the three constituents of angular velocity $\dot{\phi}, \dot{\theta}$, and $\dot{\psi}$, where $\dot{x}$ indicates the time derivative $\dot{x} = \frac{\partial x}{\partial t}$ of x. The angular velocity $\boldsymbol{\Omega}$ can be written as

$$\boldsymbol{\Omega} = \dot{\theta}\mathbf{e}_N + \dot{\phi}\mathbf{e}_z + \dot{\psi}\mathbf{e}_{(3)}, \tag{3.36}$$

where $\mathbf{e}_N$ points along the *line of nodes*, which is the intersection of the x-y-plane and the $(1)(2)-$plane

$$\mathbf{e}_N = \mathbf{e}_{(1)} \cos\psi - \mathbf{e}_{(2)} \sin\psi. \tag{3.37}$$

In the internal frame the rotation can be described with

$$\boldsymbol{\Omega} = \begin{pmatrix} \dot{\phi}\sin(\theta)\sin(\psi) + \dot{\theta}\cos(\psi) \\ \dot{\phi}\sin(\theta)\cos(\psi) + \dot{\theta}\sin(\psi) \\ \dot{\phi}\cos(\theta) + \dot{\psi} \end{pmatrix}. \tag{3.38}$$

W.l.o.g. the local z-axis can be chosen to be aligned with the magnetization for every moment so that $m = \begin{pmatrix} 0 & 0 & 1 \end{pmatrix}^T$. With ψ representing a rotation around the rotationally symmetric part of the magnetization, it can be set to a fixed angle $\psi = 0$ giving a rotational velocity vector of

$$\boldsymbol{\Omega} = \begin{pmatrix} \dot{\theta} \\ \dot{\Phi}\sin\theta \\ \dot{\Phi}\cos\theta + \dot{\Psi} \end{pmatrix}. \tag{3.39}$$

To calculate the equations of motion, the Lagrange equation

$$L = T(\mathbf{q}, \dot{\mathbf{q}}) - V(\mathbf{q}) \tag{3.40}$$

with generalized coordinates $\mathbf{q}$ and $\dot{\mathbf{q}}$ kinetic energy $T(\mathbf{q}, \dot{\mathbf{q}})$ and potential energy $V(\mathbf{q}) = E_{\text{tot}}$ can be used.

The potential energy contributions are laid out in section 3.1. The kinetic energy contribution cannot be explained classically since the magnetic moment is not connected to a tensor of inertia. However, following semi-classical kinetic energy

was chosen in [34]:

$$T(\theta, \phi, \dot{\phi}) = \int_\Omega \frac{M_S}{\gamma} \dot{\phi} \cos\theta \, \mathrm{d}^3\mathbf{r}, \tag{3.41}$$

which is equivalent to a classical rigid body rotation energy around the local magnetic axis $\mathbf{e}_{(3)}$ with $I_1 = I_2 = 0$, $I_3 = I$, and the saturation magnetization $M_S = \gamma_e L_3 = \gamma_3 I_3 \Omega_3$:

$$T(\theta, \phi, \dot{\phi}) = \int_\Omega \frac{1}{2} I(\dot{\phi}\cos\theta + \dot{\psi})^2 \, \mathrm{d}^3\mathbf{r} \tag{3.42}$$

$$= \int_\Omega \frac{1}{2} I\Omega_3^2 \, \mathrm{d}^3\mathbf{r} \tag{3.43}$$

For a more rigorous explanation see [3].

With the functional derivative $\frac{\delta}{\delta g}$ and an added dissipative Rayleigh term $\frac{\delta D}{\delta \dot{\mathbf{q}}}$, accounting for energy transfer and the generalized coordinates $\mathbf{q} = (\phi, \theta)$, the Lagrangian equation of motion reads as follows:

$$\frac{\mathrm{d}}{\mathrm{d}t} \frac{\delta L}{\delta \dot{\mathbf{q}}} - \frac{\delta L}{\delta \mathbf{q}} + \frac{\delta D}{\delta \dot{\mathbf{q}}} = 0 \tag{3.44}$$

Inserting Gilbert's Lagrangian equation (3.44) into the Lagrangian equation of motion (3.40) with the kinetic term (3.41) gives

$$-\dot{\phi}\sin(\theta) = \frac{\gamma}{M_S} \left(\frac{\delta V(\mathbf{q})}{\delta \theta} + \frac{\delta D}{\delta \dot{\theta}} \right) \tag{3.45}$$

by variation of θ, and

$$-\dot{\theta}\sin(\theta) = \frac{\gamma}{M_S} \left(\frac{\delta V(\mathbf{q})}{\delta \phi} + \frac{\delta D}{\delta \dot{\phi}} \right) \tag{3.46}$$

by variation of ϕ. To convert the equations of motion from Euler angles to Cartesian coordinates consider the time derivation of the magnetization

$$\partial_t \mathbf{m} = \mathbf{\Omega} \times \mathbf{m} = \begin{pmatrix} \dot{\phi}\sin(\theta) \\ -\dot{\theta} \\ 0 \end{pmatrix}. \tag{3.47}$$

If the normalized magnetization $|\mathbf{m}| = 1$ is considered it can be varied with respect to the Euler angles ϕ and θ as

$$\delta m_1 = \sin(\theta)\delta\phi \tag{3.48}$$

and

$$\delta m_2 = \delta\theta. \tag{3.49}$$

Inserting equations (3.45) and (3.46) into equation (3.47) and replacing the functional derivatives gives

$$\partial_t m_1 = -\frac{\gamma}{M_S}\left(\frac{\delta V}{\delta m_2} + \frac{\delta D}{\delta \dot{m}_2}\right) \tag{3.50}$$

and

$$\partial_t m_2 = \frac{\gamma}{M_S}\left(\frac{\delta V}{\delta m_1} + \frac{\delta D}{\delta \dot{m}_1}\right) \tag{3.51}$$

and combines to

$$\partial_t \mathbf{m} = \frac{\gamma}{M_S}\mathbf{m} \times \left(\frac{\delta V}{\delta \mathbf{m}} + \frac{\delta D}{\delta \dot{\mathbf{m}}}\right). \tag{3.52}$$

The Landau-Lifshitz-Gilbert [LLG] equation

$$\partial_t \mathbf{m} = \gamma(\mathbf{m} \times \mathbf{H}_{\text{eff}}) + \alpha(\mathbf{m} \times \partial_t \mathbf{m}) \tag{3.53}$$

is obtained by choosing a dissipative function D proportional to the squared rate of change of the magnetization

$$D = \frac{M_S}{2\gamma_e}\alpha(\partial_t \mathbf{m})^2, \tag{3.54}$$

with the dimensionless damping factor $\alpha \geq 0$ and the effective field $\mathbf{H}_{\text{eff}} = -\frac{1}{\mu_0 M_S}\frac{\delta V}{\delta \mathbf{m}}$.

3.2.2. Properties of the LLG Equation

Preservation of magnitude The LLG equation preserves the magnitude of the magnetization $\mathbf{m}$. This can be seen if the LLG equation (equation (3.53)) is inserted into the time dependence of the squared magnetization:

$$\partial_t |\mathbf{m}|^2 = \partial_t (\mathbf{m} \cdot \mathbf{m}) = 2(\partial \mathbf{m}) \cdot \mathbf{m} \tag{3.55}$$

$$\frac{1}{2}\partial_t |\mathbf{m}|^2 = -\gamma(\mathbf{m} \times \mathbf{H}_{\text{eff}}) \cdot \mathbf{m} + \alpha(\mathbf{m} \times \partial_t \mathbf{m}) \cdot \mathbf{m} = 0 \tag{3.56}$$

Lyapunov Structure For a stationary energy functional (i.e., time-independent field) the temporal dependence of the energy density U can be written as

$$\partial_t U = \frac{\delta U}{\delta \mathbf{m}} \cdot \partial_t \mathbf{m} = -\mu_0 M_S \mathbf{H}_{\text{eff}} \cdot \partial_t \mathbf{m}. \tag{3.57}$$

Inserting the LLG equation gives

$$\partial_t U = -\mu_0 M_S \mathbf{H}_{\text{eff}} \cdot \left(-\gamma'(\mathbf{m} \times \mathbf{H}_{\text{eff}}) - \alpha' \mathbf{m} \times (\mathbf{m} \times \mathbf{H}_{\text{eff}})\right) \tag{3.58}$$

$$= \mu_0 M_S \mathbf{H}_{\text{eff}} \cdot (\alpha' \mathbf{m} \times (\mathbf{m} \times \mathbf{H}_{\text{eff}})) \tag{3.59}$$

$$= \mu_0 M_S \alpha' \mathbf{H}_{\text{eff}} \cdot \left((\mathbf{m} \cdot \mathbf{H}_{\text{eff}})\mathbf{m} - \mathbf{H}_{\text{eff}}|m|^2)\right) \tag{3.60}$$

$$= \mu_0 M_S \alpha' \left(|(\mathbf{m} \cdot \mathbf{H}_{\text{eff}})|^2 - |\mathbf{H}_{\text{eff}}|^2 |m|^2)\right) \leq 0, \tag{3.61}$$

a non-increasing time dependence of the energy functional over time (i.e., Lyapunov Structure [35, 36]).

Hamiltonian Structure For a vanishing damping term in the LLG equation (i.e., $\alpha' = 0$), the time dependence of the energy functional

$$\partial_t U = 0 \tag{3.62}$$

vanishes in equation (3.61). In other words, the energy is conserved, and the LLG equation has Hamiltonian structure.

3.2.3. Applicability and Improvements of the Micromagnetic Model

The micromagnetic model is a well-tested tool for the study of magnetism. Still, it is a simplified model and not a panacea for every problem domain. This section discusses some caveats of and extensions to the micromagnetic model for deepening the understanding of its applicability and validity without any claims to completeness.

Bloch Points   [37] showed that in ferromagnetic materials singularities with a significant change in the direction of $\mathbf{m}$ between neighboring moments exist. These singularities are called Bloch points. An example of a Bloch point is the center of a sphere with a hedgehog-like magnetization where no direction for the magnetization exists. This means that the underlying micromagnetic assumption that a continuous function $\mathbf{m}(\mathbf{r})$ with constant saturation magnetization M_S cannot describe the magnetization.

Nonetheless, [38, 39] show that the Bloch points can be described in the framework of micromagnetic simulations in agreement with experimental results, albeit underestimating the energy density near the Bloch points.

Thermal Fluctuations   Thermal fluctuations again violate the continuity of the magnetization $\mathbf{m}(\mathbf{r})$ by perturbing it locally. Several approaches to solving this problem exist. A mean-field approximation reduces the saturation magnetization $M_S(T)$ as a function of temperature, posing only a minor modification to the framework of micromagnetic theory (see [40]).

The introduction of a randomly fluctuating field as an additional term in the effective field $\mathbf{H}_{\text{eff}}$ turns the LLG equation into a stochastic differential equation (see [41]).

Spin-Polarized Currents   Spin-polarized currents give rise to a branch of magnetism called spintronics. In spintronics, currents can be manipulated by spin and charge instead of only by charge [42]. This effect results from the band structure of ferromagnetic solids like Fe, Co, Ni and their alloys. The band structure causes the population of one spin direction to be larger than the other. In contrast, most materials have an equal population of spin-up and spin-down electrons. To picture a spin-polarized current one can start by imagining a current flowing through a magnetic solid, the resistance for electrons would then be dependent on their polarization, and thus a difference in resistance between spin-up and spin-down electrons would occur. This spin asymmetry creates various spin-related transport phenomena. Since the discovery of the GMR effect [43] many technological and scientific applications have taken advantage of spin-polarized currents. A model for describing spin-polarized currents in a micromagnetic context is given in [44].

Interfacial Effects   The micromagnetic model assumes a homogeneous solid, but many magnetic effects happen at the interfaces between different materials. These effects often have a quantum mechanical origin like the Ruderman-Kittel-Kasuya-Yosida [RKKY] interaction [45] and the Dzyaloshinskii-Moriya interaction [DMI] [46]. A commonly used simplification is the use of experimentally measured *effective* material constants. Another way is to integrate the physicals directly in the model as is done in [47, 48, 49].

4. FMM

The Fast Multipole Method [FMM] was first presented by [50] and later chosen as one of the top algorithms of the 20th century by [51]. The original implementation used point-like sources, whereas the presented implementation works on linearly varying continuous sources (see section 4.2). The FMM uses direct evaluation of the field or potential, making it part of the same category of algorithms as Fast Fourier Transform [FFT] [52], non-uniform FFT [NUFFT] [53] and tensor grid methods [54]. Compared to the FFT, the FMM is an approximate algorithm and does not require a regular grid. This means, it has less precision and the possibility to be used in conjunction with the finite element method. On top of that FMM scales better to larger systems than FFT ($\mathcal{O}(N)$ compared to $\mathcal{O}(N \log N)$).

A naive implementation of the discretized (see section 4.2) stray field needs to compute the interaction between each source and target point $NE \cdot N \propto N^2$. Some prerequisite knowledge is necessary to understand the FMM algorithm. The next sections explain the expansions (section 4.4.1, section 4.4.2) for approximating sources, targets (section 4.4.3), and how to convert and reuse these (section 4.4.4). First, a simpler $N \log(N)$ algorithm spanning one dimension, requiring only source expansions and exhibiting a simpler tree structure, is presented in section 4.5. The simplified algorithm is then refined into the full three-dimensional continuous linearly scaling (N) algorithm in section 4.6.

4.1. Definitions

The definition of barycentric coordinates and polynomial spaces are needed for the following sections.

A tetrahedron $T \subset \mathbb{R}^3$ is the convex hull of four points $\mathbf{x}^i \in \mathbb{R}^3$ that form the vertices of T.

Barycentric coordinates λ of $\mathbf{x} \in T$ are a parametrization of T using a convex combination of the vertices $\mathbf{x}^i$:

$$T = \left\{ \mathbf{x} \in \mathbb{R}^3 : \mathbf{x} = \sum_{i=1}^{4} \lambda_i \mathbf{x}^i, 0 \leq \lambda_i \leq 1, \sum_{i=1}^{4} \lambda_i = 1 \right\} \tag{4.1}$$

The barycentric coordinates of the vertex $\mathbf{x}^i$ are $\lambda_i = 1$ and $\lambda_j = 0$, $\forall j \neq i$. The barycentric coordinate λ_i can be identified by the linear function that is 1 at the vertex $\mathbf{x}_i$ and vanishes at all other vertices $\mathbf{x}^j \neq \mathbf{x}^i$.

The transformation of barycentric to Cartesian coordinates can be done with the components of $\mathbf{x}^i = (x_i, y_i, z_i)$

$$x = \lambda_1 x_1 + \lambda_2 x_2 + \lambda_3 x_3 + \lambda_4 x_4, \tag{4.2}$$

$$y = \lambda_1 y_1 + \lambda_2 y_2 + \lambda_3 y_3 + \lambda_4 y_4, \tag{4.3}$$

$$z = \lambda_1 z_1 + \lambda_2 z_2 + \lambda_3 z_3 + \lambda_4 z_4, \tag{4.4}$$

where $\lambda_4 = 1 - \lambda_1 - \lambda_2 - \lambda_3$. The inverse transformation can be done by solving the system of equations (4.2) to (4.4) for λ_1, λ_2, and λ_3.

For the definition of the polynomial space P_k consider the following. Let $\mathbf{r} \in \mathbb{R}^3$, and $\alpha \in \mathbb{N}_+$, then the polynomial space P_k is given as:

$$P_k = \text{span} \left\{ \prod_{i=1}^{3} r_i^{\alpha_i} \text{ for } i = 1, 2, 3, \ \sum_{i=1}^{3} \alpha_i \leq k \right\} \tag{4.5}$$

4.2. Discretization

For the application of the FMM, it is necessary to use a discrete function space on the problem domain Ω. A choice for using finite element function spaces is made to be compatible with existing finite element software based on [55]. The source space $V = \{\mathbf{M} \in H^1(\Omega)\}$ restricts sources $\mathbf{M}$ to a discrete space $V_H \subset V$ with discrete sources $\mathbf{M}_i \in V_H$.

$$u_H(\mathbf{r}_t) = -\frac{1}{4\pi} \int_\Omega \mathbf{M}_i(\mathbf{r}_s) \cdot \nabla_s \frac{1}{|\mathbf{r}_t - \mathbf{r}_s|} \, \mathrm{d}^3\mathbf{r}_s, \tag{4.6}$$

where $\mathbf{r}_t$ are the target points and $\mathbf{r}_s$ are the source points.

A tetrahedral mesh can be created by partitioning the domain Ω into a finite set of tetrahedra $\mathcal{T}_h = \{T\}$ with disjoint interiors such that $\cup_{T \in \mathcal{T}_h} T = \Omega$.

4.2.1. Finite Element Definition

The finite element definition was first brought forward by [56]. To create a finite element a local function space $\mathcal{V}$ is defined on each partitioned cell T. The function space V_H is populated by patching together (linear) functions. To create a finite element a combination of a cell T plus a local function space $\mathcal{V}$ and the rules for describing functions in the function space $\mathcal{V}$ is needed. A more formal definition by [55] is reprinted below:

The finite element is a triple $(T, \mathcal{V}, \mathcal{L})$ where

- the domain T is a bounded, closed subset of $\mathbb{R}^d$ (for $d = 1, 2, 3, \dots$) with nonempty interior and piecewise smooth boundary;
- the space $\mathcal{V} = \mathcal{V}(T)$ is a finite-dimensional function space on T of dimension n;
- the set of degrees of freedom (node values) $\mathcal{L} = \{\ell_1, \ell_2, \dots, \ell_n\}$ is a basis for the dual space $\mathcal{V}'$; that is, the space of bounded linear functionals on $\mathcal{V}$.

As an example consider the Lagrangian finite element on the triangle. The cell T is given by the triangle and the space $\mathcal{V}$ is given by the first-degree polynomials P_1 on T. For the dual basis point-wise evaluation can be used:

$$l_i : \mathcal{V} \to \mathbb{R} \tag{4.7}$$

$$l_i(\nu) = \nu(\mathbf{x^i}) \tag{4.8}$$

for $i \in \{1, 2, 3, 4\}$, where $\mathbf{x}^i$ is the coordinate of the ith vertex and ν a function in $\mathcal{V}$.

The choice used in this thesis for sources $\mathbf{m}_i$ is the linear Lagrange finite element on the tetrahedron. The cell T is given by the tetrahedron and $\mathcal{V} := P_k^3$ is the 3d-space of first-degree polynomials P_k^3 with $\nu \in \mathcal{V}$ on T. The dual basis is the magnetization $\mathbf{M}_i$. For the dual space $\mathcal{V}'$ point evaluation at the four tetrahedral vertices is used:

$$\mathbf{M}_i : \mathcal{V}' \to \mathbb{R}^3, \tag{4.9}$$

$$\mathbf{M}_i = \mathbf{M}(\mathbf{x}^i) \tag{4.10}$$

for $i \in \{1, 2, 3, 4\}$, where $\mathbf{x}^i$ is the coordinate of the ith vertex.

4.2.2. Discretized Function Spaces

The FMM function space discretizes the target space u as a discrete space $u_H(\mathbf{x}) \in V_H$ with discretization points $\mathbf{x}^i$ such that

$$u_H(\mathbf{x}^i) = u(\mathbf{x}^i) \forall \mathbf{x}^i. \tag{4.11}$$

The cell T is a tetrahedron and the space $V_H = P_1$ is the first degree polynomial space on T (see figures 4.1 and 4.2).

To simplify the basis functions a *nodal basis* can be used for the local basis function space $\mathcal{V}_H$. The nodal basis $\{\phi_i\}_{i=1}^n$ for $\mathcal{V}_H$ satisfies
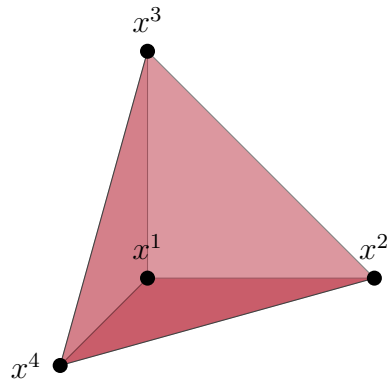
Figure 4.1.: The linear Lagrange tetrahedron has four degrees of freedom corresponding to its four vertices x^i.
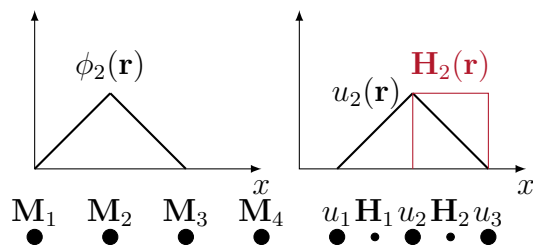

Figure 4.2.: A one-dimensional sketch of the discretization of magnetization $\mathbf{M}$, potential u, and field $\mathbf{H}$ as linear or constant Lagrange intervals.

$$l_i(\phi_j) = \delta_{ij}, \quad i,j = 1,2,\ldots,n \tag{4.12}$$

so that any function $\nu \in \mathcal{V}_H$ can be written as

$$\nu = \sum_{i=1}^{n} l_i(\nu)\phi_i. \tag{4.13}$$

In the case of the tetrahedral Lagrange element the nodal basis is given as

$$\phi_i(x) = \lambda_i, \tag{4.14}$$

using barycentric coordinates (see section 4.1).

In summary, this means the magnetization DOFs $\mathbf{M}_i, u_i \in V_H \subset H^1(\Omega)$ are defined node-wise as piecewise affine globally continuous functions. Whereas the field values $\mathbf{H}_i$ are defined cell-wise as piecewise constant globally discontinuous functions with evaluation points at cell centers as seen in figure 4.2.

4.3. Direct Integration

The Fast Multipole Method uses the singular volume integral for the potential (see equation (3.20)) and the field (see equation (3.22)). A straightforward solution uses the conjunct integral form $u(\mathbf{r}_t) = \frac{1}{4\pi} \int_\Omega \mathbf{M}(\mathbf{r}_s) \cdot \nabla_t \frac{1}{|\mathbf{r}_t - \mathbf{r}_s|} \,\mathrm{d}^3\mathbf{r}_s$ by transforming the tetrahedron into a prism and lifting the geometric singularity at $\mathbf{r}_s = \mathbf{r}_t$ similar to [57] which is in turn based on [58]. The resulting surface integrals can then be integrated analytically or numerically depending on the speed of execution. The details for this solution are given in section 3.1.2.

The implementation in chapter 6 uses the disjunct equations (3.21) and (3.22). The reasoning for using the disjunct form goes as follows: Two neighboring discretization tetrahedra T_i and T_j share a surface triangle $\Delta_{il} = -\Delta_{jk}$ with opposite normal vector $\mathbf{n}_i = -\mathbf{n}_j$, and thus the contributions cancel for all cell surfaces except geometric boundaries. Canceling terms can cause numerical problems—if the surface terms are dominant compared to the volume terms—in two ways. First, when using FMM the error is proportional to the expanded integral, making its absolute value larger for large canceling surface contributions. Second, because of subtraction in the near field. Subtracting two identical but large numbers leads to a loss of precision (i.e., an increase of error). For completeness, the integrals solving the conjunct integral are given in section 4.3.2.

4.3.1. Triangle Integrals

The solution of the tetrahedral singular integrals in the next sections lead to triangular single-layer potentials E_{jk} and double-layer potentials D_{jk} with polynomial

support $x^j y^k$.

$$E_{jk} = \frac{1}{4\pi} \int_\Delta \frac{x^j y^k}{\sqrt{x^2 + y^2 + z_t^2}} \, \mathrm{d}x \, \mathrm{d}y \tag{4.15}$$

$$D_{jk} = \frac{z_t}{4\pi} \int_\Delta \frac{x^j y^k}{\left(x^2 + y^2 + z_t^2\right)^{\frac{3}{2}}} \, \mathrm{d}x \, \mathrm{d}y, \tag{4.16}$$

where z_t is the normal distance of the evaluation point $\mathbf{r}_t$, and the evaluation point is assumed to be on the z-axis ($x_t = y_t = 0$). This section shows the necessary formulas and an overview of the derivation for an analytic solution described in [59] to integrate these.

With the divergence theorem, the vector field $G = 1/r(x, y)^T \Rightarrow \mathrm{div} G = 1/r + z_t^2/r^3$, and $r = (x^2 + y^2 + z_t^2)$ a reduction of E_{jk} and D_{jk} to D_{00} and line integrals $E_{jk}^{(\gamma)}$ along the edges γ of the triangle Δ is possible (see equation (4.42)).

$$E_{jk}^{(\gamma)} = \frac{1}{4\pi} \int_\gamma \frac{x^j y^k}{\sqrt{x^2 + y^2 + z_t^2}} \, \mathrm{d}\gamma \tag{4.17}$$

Both D_{00} and $E_{jk}^{(\gamma)}$ are analytically solvable.

Double-Layer Potential with Constant Carrier   Starting with the double-layer potential $D_{00}(\mathbf{r}_t, T)$ over the triangle T with a constant carrier and an evaluation point $\mathbf{r}_t = (0, 0, z_t)^T$, the double-layer potential is given as

$$\frac{D_{00}(\mathbf{r}_t, T)}{z_t} = \frac{1}{4\pi} \int_T \nabla_t \frac{1}{\|\mathbf{r}_s - \mathbf{r}_t\|^3} \, \mathrm{d}^3\mathbf{r}_s = \frac{1}{4\pi} \int_T \frac{\hat{\mathbf{n}} \cdot (\mathbf{r}_s - \mathbf{r}_t)}{\|\mathbf{r}_s - \mathbf{r}_t\|^3} \, \mathrm{d}^2\mathbf{r}_t. \tag{4.18}$$

The double-layer potential can be identified with the area of the spherical triangle created by projection of T on the unit sphere $S_1(\mathbf{r}_t)$ [60, 61, 59]:

$$\Delta_K = \left\{ \mathbf{x} \in S_1(\mathbf{r}_t) : \exists \mathbf{r} \in T, \text{so that } \mathbf{x} \in \overline{\mathbf{r}_t \mathbf{r}} \right\} \tag{4.19}$$

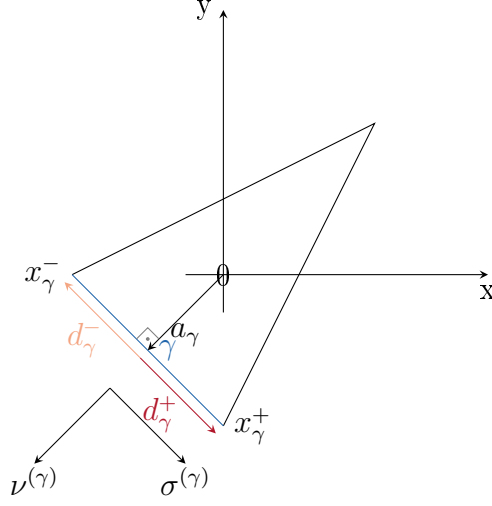$$D_{00}(\mathbf{r}_t, T) = \frac{|z_t|}{4\pi} |\Delta_K| \tag{4.20}$$

Figure 4.3.: Sketch of an arbitrarily chosen side $\gamma \in \{1, 2, 3\}$ of the rotated triangle Δ. The figure shows the frame (ν, σ) of γ, its integration boundaries $x_\gamma^\pm$, and other variables used for the integration of the solid angle $|\Delta_K|$.

For the lengthy solution of the solid angle Δ_K w.l.o.g. the singular integral region has been rotated into the x-y-plane with the normal vector $n = (0, 0, 1)$ evaluating the dot product $\mathbf{n} \cdot (\mathbf{r}_s - \mathbf{r}_t) = z_t$ as the z-component of the evaluation point $\mathbf{r}_t$. The line integrals C_γ can be calculated using the following geometric variables: the edge γ denoting any one edge of the triangle Δ, the reference frame for integration along γ, where $\nu^{(\gamma)}$ is the normal vector, and $\sigma^{(\gamma)}$ the tangential vector to γ, and the integration endpoints x_γ^+ following after x_γ^- by orienting γ with $\sigma^{(\gamma)}$ (see figure 4.3). With

$$a_\gamma := \mathbf{r} \cdot \nu^{(\gamma)}, \mathbf{r} \in \gamma, \qquad (4.21)$$

$$d_\gamma^\pm := x_\gamma^\pm \cdot \sigma^{(\gamma)}, \qquad (4.22)$$

$$e_\gamma := \sqrt{z_t + a_\gamma^2}, \qquad (4.23)$$

$$s_\gamma^\pm := \sqrt{e_\gamma^2 + d_\gamma^{\pm 2}}, \qquad (4.24)$$

and the definition of C_γ [62]

$$c_\gamma^\pm := e_\gamma^2 + |z_t|s_\gamma^\pm \tag{4.25}$$

$$A\gamma := c_\gamma^+ c_\gamma^- + a_\gamma^2 d_\gamma^+ d_\gamma^- \tag{4.26}$$

$$B_\gamma := a_\gamma(d_\gamma^+ c_\gamma^- - d_\gamma^- c_\gamma^+) \tag{4.27}$$

$$C_\gamma := \mathrm{atan2}(B_\gamma, A_\gamma) \tag{4.28}$$

the solid angle $|\Delta_K|$ is given by

$$|\Delta_K| = \begin{cases} \sum_\gamma C_\gamma & \text{for } x \neq 0 \\ 0 & \text{otherwise} \end{cases}. \tag{4.29}$$

Single-Layer and Double-Layer Potential Higher order polynomial carriers can be recursively calculated using the double-layer potential with a constant carrier D_{00}.

$$E_{jk} = \frac{1}{4\pi} \int_\Delta \frac{x^j y^k}{\sqrt{x^2 + y^2 + z_t^2}} \, \mathrm{d}x \, \mathrm{d}y \tag{4.30}$$

$$D_{jk} = \frac{z_t}{4\pi} \int_\Delta \frac{x^j y^k}{(x^2 + y^2 + z_t^2)^{\frac{3}{2}}} \, \mathrm{d}x \, \mathrm{d}y \tag{4.31}$$

The triangular integrals are reduced to line integrals $E_{jk}^{(\gamma)}$ using the divergence theorem.

$$E_{jk}^{(\gamma)} := \frac{1}{4\pi} \int_\gamma \frac{x^j y^k}{\sqrt{x^2 + y^2 + z_t^2}} \, \mathrm{d}\gamma \tag{4.32}$$

The line integrals $E_{jk}^{(\gamma)}$ can be calculated analytically (proof see [59]):

$$E_{00}^{(\gamma)} = \begin{cases} \frac{1}{4\pi} \log \left(\frac{(s_\gamma^- - d_\gamma^-)s_\gamma^+ + d_\gamma^+}{e_\gamma^2} \right) & \text{for } e_\gamma \neq 0 \\ \frac{1}{4\pi} \log \left(\frac{\max(|d_\gamma^+|, |d_\gamma^-|)}{\min(|d_\gamma^+|, |d_\gamma^-|)} \right) & \text{for } e_\gamma = 0 \end{cases} \tag{4.33}$$

4. FMM

For $|\nu_1^{(\gamma)}| \geq |\nu_2^{(\gamma)}|$, where $\nu_1^{(\gamma)}$ and $\nu_2^{(\gamma)}$ are the x and y-components of $\nu^{(\gamma)}$

$$E_{0k}^{(\gamma)} = \frac{1}{k} \left((2k-1)a_\gamma \nu_2^{(\gamma)} E_{0,k-1}^{(\gamma)} - (k-1)(a_\gamma^2 + (z_t \nu_1^{(\gamma)})^2) E_{0,k-2}^{(\gamma)} \right. \tag{4.34}$$

$$\left. + \nu_1^{(\gamma)} G_{0,k-1}^{(\gamma)} \right) \text{ for } k \geq 1 \tag{4.35}$$

$$E_{jk}^{(\gamma)} = \left(a_\gamma E_{j-1,k}^{(\gamma)} - \nu_2^{(\gamma)} E_{j-1,k+1}^{(\gamma)} \right) / \nu_1^{(\gamma)} \text{ for } j \geq 1 \tag{4.36}$$

and for $|\nu_1^{(\gamma)}| < |\nu_2^{(\gamma)}|$

$$E_{j0}^{(\gamma)} = \frac{1}{j} \left((2j-1)a_\gamma \nu_1^{(\gamma)} E_{j-1,0}^{(\gamma)} \right. \tag{4.37}$$

$$- (j-1) \left(a_\gamma^2 + (z_t \nu_2^{(\gamma)}))^2 \right) E_{j-2,0}^{(\gamma)} \tag{4.38}$$

$$\left. - \nu_2^{(\gamma)} G_{j-1,0}^{(\gamma)} \right) \text{ for } j \geq 1 \tag{4.39}$$

$$E_{jk}^{(\gamma)} = \left(a_\gamma E_{j,k-1}^{(\gamma)} - \nu_1^{(\gamma)} E_{j+1,k-1}^{(\gamma)} \right) / \nu_2^{(\gamma)} \text{ for } k \geq 1 \tag{4.40}$$

with

$$G_{jk}^{(\gamma)} = \frac{1}{4\pi} \left((x_\gamma^+)^j (y_\gamma^+)^k s_\gamma^+ - (x_\gamma^-)^j (y_\gamma^-)^k s_\gamma^- \right). \tag{4.41}$$

And finally, the *triangle potentials* for $\mathbf{r}_t \in \mathbb{R}^3 \setminus T$ with $E_{0,-1} := 0$.

$$E_{00} = -z_t D_{00} + \sum_\gamma a_\gamma E_{00}^{(\gamma)} \tag{4.42}$$

$$E_{0k} = \frac{1}{k+1}\left\{ z_t^2(1-k)E_{0,k-2} + \sum_\gamma \left(z_t \nu_2^{(\gamma)} E_{0,k-1}^{(\gamma)} + a_\gamma E_{0k}^{(\gamma)} \right) \right\}, k \geq 1 \tag{4.43}$$

$$\begin{aligned} E_{jk} =& \frac{1}{j+k+1}\Big(-z_t^2(j-1)E_{j-2,k} \\ &+ \sum_\gamma (z_t^2 \nu_1^{(\gamma)} E_{j-1,k}^{(\gamma)} + a_\gamma E_{jk}^{(\gamma)}) \Big), k \geq 0, j \geq 1 \end{aligned} \tag{4.44}$$

$$D_{0k} = -z_t \left\{ (1-k)E_{0,k-2} + \sum_\gamma \nu_2^{(\gamma)} E_{0,k-1}^{(\gamma)} \right\}, k \geq 1 \tag{4.45}$$

$$D_{1k} = -z_t \sum_\gamma \nu_1^{(\gamma)} E_{0k}^{(\gamma)}, k \geq 0 \tag{4.46}$$

$$D_{jk} = -D_{j-2,k+2} - z_t^2 D_{j-2,k} + z_t E_{j-2,k}, j \geq 2, k \geq 0 \tag{4.47}$$

4.3.2. Direct Conjunct Integral

This section explains the integration of the conjunct (i.e., not surface plus volume term) integral form for the potential over tetrahedron T:

$$u(\mathbf{r}_t) = \frac{1}{4\pi} \int_T \mathbf{M}(\mathbf{r}_s) \cdot \nabla_t \frac{1}{|\mathbf{r}_t - \mathbf{r}_s|} \, \mathrm{d}^3 \mathbf{r}_s \tag{4.48}$$

As mentioned before, this solution is based on [57] which is in turn based on [63, 58]. In the first step, the tetrahedron is split into four tetrahedra. Each vertex of the original tetrahedron is successively replaced with the target, resulting in four tetrahedral integration regions with one vertex $\mathbf{x}^i = \mathbf{r}_t$ (see figure 4.4): W.l.o.g. the frame of reference can be chosen such that $\mathbf{r}_t$ lies on the z-axis and the other three vertices on the x-y-plane (see figure 4.5).
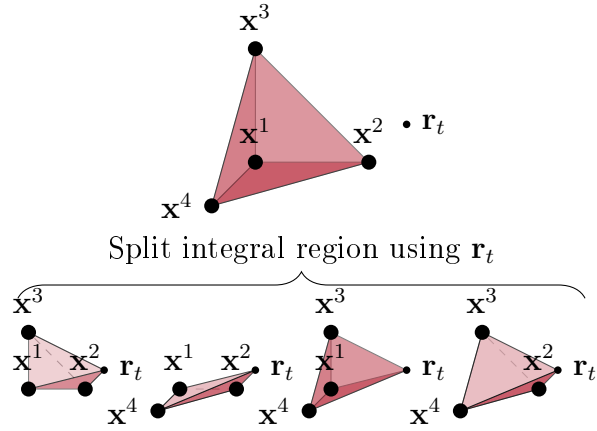
Figure 4.4.: A tetrahedron is split into four tetrahedra so that the new integration regions all have the evaluation point $\mathbf{r}_t$ coinciding with an integration vertex.
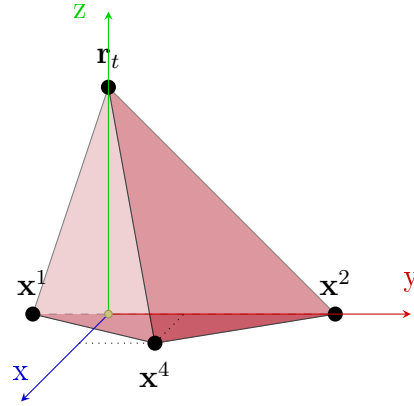

Figure 4.5.: The tetrahedron is transformed so that the x- and y-components of $\mathbf{r}_{tx} = \mathbf{r}_{ty} = 0$ are zero and the z-component of the remaining vertices $v_{iz} = 0$ are zero.

The magnetization $\mathbf{M}(\mathbf{r}) = \sum_i \mathbf{M}_i \Phi_i$ inside the tetrahedron T can be written as an affine function using an augmented (i.e., 3x4) matrix A_{jk} (see [64])

$$M_j(\mathbf{r}) = \sum_k A_{jk} I_k(\mathbf{r}), \qquad (4.49)$$

where $M_j(\mathbf{r})$ are the x-, y-, and z-components of $\mathbf{M}(\mathbf{r})$, r_i are the components of $\mathbf{r}$, and $I_k(\mathbf{r}) = \begin{pmatrix} 1 \\ r_x \\ r_y \\ r_z \end{pmatrix}$. A_{jk} can be solved with the linear set of equations using the magnetization $\mathbf{M}_j$ at the four vertices $\mathbf{x}^i$ of T, giving four equations for each component of $\mathbf{M}$:

$$M_j(\mathbf{x}^i) = A_{jk} I_k(\mathbf{x}^i) \qquad (4.50)$$

The resulting integrations use the components r_{tj} of the target point $\mathbf{r}_t$ and r_{sj} of the source point $\mathbf{r}_s$:

$$u(\mathbf{r}_t) = \frac{1}{4\pi} \sum_{j,k} A_{jk} \int_T I_k(\mathbf{r}_s) \frac{r_{tj} - r_{sj}}{|\mathbf{r}_t - \mathbf{r}_s|^3} \, \mathrm{d}^3\mathbf{r}_s \qquad (4.51)$$

All integrals have a singularity at the evaluation corner $\mathbf{r}_t = \mathbf{r}_s$ which can be resolved by following non-linear Duffy transformation [58, 63, 57]

$$r_{sx} = x_s \to x_s'(1 - \lambda) \qquad r_{sy} = y_s \to y_s'(1 - \lambda) \qquad \frac{r_{sz}}{r_{tz}} = \frac{z_s}{z_t} \to \lambda \qquad (4.52)$$

with Jacobian

$$J = z_t(1 - \lambda)^2. \qquad (4.53)$$

The transformation gives a new integration region, namely the prism $\int_T \to \int_\Delta \int_0^{z_t}$ over the base triangle Δ of the tetrahedron T with its height $z_t = r_{tz}$. With $\mathbf{r}_t$ being at height z_t, the distance

$$|\mathbf{r}_t - \mathbf{r}_s| = \sqrt{x_s^2 + y_s^2 + (z_t - z_s)^2} \qquad (4.54)$$

53

becomes

$$|\mathbf{r}_t - \mathbf{r}_s| \to \sqrt{x'^2(1-\lambda)^2 + y'^2(1-\lambda)^2 + z_t^2(1-\lambda)^2} = (1-\lambda)\sqrt{x'^2 + y'^2 + z_t^2}.$$
(4.55)

and with $d = \sqrt{x_t^2 + y_t^2 + z_t^2}$ and the basis vectors $\hat{x}, \hat{y}$, and $\hat{z}$ the Coulomb kernel transforms as

$$\nabla \frac{1}{|\mathbf{r}_t - \mathbf{r}_s|} = \frac{\mathbf{r}_t - \mathbf{r}_s}{\|\mathbf{r}_t - \mathbf{r}_s\|^3} \to \frac{1-\lambda}{(1-\lambda)^3} \frac{x_s\hat{x} + y_s\hat{y} + \hat{z}}{d^3}$$
(4.56)

and finally gives the potential

$$
\begin{aligned}
u(\mathbf{r}_t) &= -\frac{z_t}{4\pi} A_{jk} \int_\Delta \int_0^1 \frac{x_s\delta_{\hat{x}j} + y_s\delta_{\hat{y}j} + z_t\delta_{\hat{z}j}}{d^3} I_k \, \mathrm{d}z_s \, \mathrm{d}^2\mathbf{r}_s \\
&= -\frac{z_t}{4\pi} A_{jk} \int_\Delta \frac{x_s\delta_{\hat{x}j} + y_s\delta_{\hat{y}j} + z_t\delta_{\hat{z}j}}{(x_t^2 + y_t^2 + z_t^2)^{3/2}} I'_k \, \mathrm{d}^2\mathbf{r}_s,
\end{aligned}
$$
(4.57)

using $\delta_{\hat{x}k}$ for indicating one component of k and

$$I'_k = \begin{pmatrix} 1 \\ x_s \\ y_s \\ 1 \end{pmatrix}.$$
(4.58)

The remaining triangle integrals with a polynomial carrier are solved in section 4.3.1.

4.3.3. Disjunct Potential Integral

The conjunct potential integral for a tetrahedron can be disjoined into a volume $\int_T$ and surface contribution $\int_{\partial T}$:

$$u(\mathbf{r}_t) = \underbrace{\frac{1}{4\pi} \int_T \frac{\nabla_s \cdot \mathbf{M}(\mathbf{r}_s)}{|\mathbf{r}_t - \mathbf{r}_s|} \, \mathrm{d}^3\mathbf{r}_s}_{u_T} - \underbrace{\frac{1}{4\pi} \int_{\partial T} \frac{\mathbf{M}(\mathbf{r}_s) \cdot \mathbf{n}(\mathbf{r}_s)}{|\mathbf{r}_t - \mathbf{r}_s|} \, \mathrm{d}^2\mathbf{r}_s}_{u_{\partial T}}$$
(4.59)

Volume Term   To integrate the volume term u_T the transformations from the previous section are used to arrive at four triangle integrals. The linear magnetization $\mathbf{M}$ leads to a constant divergence $\hat{D} = \nabla_s \cdot \mathbf{M}(\mathbf{r}_s)$ which can be moved outside the integral and transformed via Duffy transformation (see section 4.3.2):

$$
\begin{aligned}
u_T(\mathbf{r}_t) &= \frac{\hat{D}}{4\pi} \int_T \frac{1}{|\mathbf{r}_t - \mathbf{r}_s|} \, \mathrm{d}^3\mathbf{r}_s \\
&= \frac{\hat{D}}{4\pi} \frac{z_t}{2} \int_{\partial T} \left(x_s^2 + y_s^2 + z_t^2\right)^{-\frac{1}{2}} \mathrm{d}x_s \, \mathrm{d}y_s
\end{aligned}
\tag{4.60}
$$

The integral over the surface triangles ∂T can be identified with the single-layer potential from section 4.3.1

$$
E_{jk} = \frac{1}{4\pi} \int_\Delta \frac{x^j y^k}{\sqrt{x^2 + y^2 + z_t^2}} \, \mathrm{d}x \, \mathrm{d}y
\tag{4.61}
$$

$$
u_T(\mathbf{r}_t) = -\hat{D} E_{00}(\partial T),
\tag{4.62}
$$

where $E_{00}(\partial T) = \sum_j E_{00}(\Delta_i)$ is the sum over all four surface triangles Δ_i of T.

Surface Term   For the surface integral $u_{\partial T}$ of the tetrahedron T w.l.o.g. vertex positions $\mathbf{x}^1 = (0,0,0)^T$, $\mathbf{x}^2 = (v_{2x}, 0, 0)$, and $\mathbf{x}^3 = (v_{3x}, v_{3y}, 0)$ can be assumed for each surface triangle Δ_i, simplifying the calculation of the function $\mathbf{M}(\mathbf{r}_s) \cdot \mathbf{n}(\mathbf{r}_s) = m_x x_s + m_y y_s + m_c$, which is linear on each surface triangle Δ_i:

$$
u_{\partial T}(\mathbf{r}_t) = -\frac{1}{4\pi} \sum_i \int_{\Delta_i} \frac{m_x x_s + m_y y_s + m_c}{|\mathbf{r}_t - \mathbf{r}_s|} \, \mathrm{d}^2\mathbf{r}_s
\tag{4.63}
$$

W.l.o.g the normal magnetization $\mathbf{M}(\mathbf{x}^i) \cdot \mathbf{n} = \delta_{1i}$ can be set to zero at all vertices but $\mathbf{x}^1$, giving:

$$
m_c = \mathbf{M}(\mathbf{x}^1) \cdot \mathbf{n}
\tag{4.64}
$$

$$
m_x = -\frac{m_c}{v_{2x}}
\tag{4.65}
$$

$$
m_y = -\frac{m_x v_{3x} - m_c}{v_{3y}} = m_c \frac{v_{3x} - v_{2x}}{v_{2x} v_{3y}}
\tag{4.66}
$$

4. FMM

To get rid of $\mathbf{r}_t$ in $\frac{1}{|\mathbf{r}_t - \mathbf{r}_s|}$ the following substitution is made:

$$x_s \to x_s + x_t, \text{ and } y_s \to y_s + y_t \tag{4.67}$$

Giving the surface term in a form that can easily be calculated with the single-layer potential from section 4.3.1:

$$u_{\partial T}(\mathbf{r}_t) = -\frac{1}{4\pi} \sum_i \int_{\Delta_i} \frac{m_x(x_t + x_s) + m_y(y_t + y_s) + m_c}{\sqrt{x_s^2 + y_s^2 + z_t^2}} \, \mathrm{d}^2\mathbf{r}_s \tag{4.68}$$

$$= -\sum_{\Delta_i} \left(m_x(E_{00}x_t + E_{10}) + m_y(E_{00}y_t + E_{01}) + m_{nc}E_{00} \right), \tag{4.69}$$

where $\sum_{\Delta_i}$ indicates which triangle is used for the single-layer potential $E_{jk} = E_{jk}(\Delta_i)$.

4.3.4. Disjunct Field Integral

Similar to the previous section, the field is disjoined into a surface and a volume contribution. The divergence of the magnetization $\nabla_s \cdot \mathbf{M}(\mathbf{r}_s) = \hat{D}$ is piecewise constant for linear piecewise affine $\mathbf{M}(\mathbf{r}_t)$.

$$\mathbf{H}(\mathbf{r}_t) = -\nabla_t u(\mathbf{r}_t) = -\frac{1}{4\pi}\nabla_t \int_T \left(\mathbf{M}(\mathbf{r}_s) \cdot \nabla_s \frac{1}{|\mathbf{r}_s - \mathbf{r}_t|} \right) \mathrm{d}^3\mathbf{r}_s \tag{4.70}$$

Applying the divergence theorem on $\int_T \left(\mathbf{M}(\mathbf{r}_s) \cdot \nabla_s \frac{1}{|\mathbf{r}_s - \mathbf{r}_t|} \right) \mathrm{d}^3\mathbf{r}_s$ gives:

$$\mathbf{H}(\mathbf{r}_t) = -\frac{1}{4\pi} \left[\nabla_t \int_T \hat{D} \frac{1}{|\mathbf{r}_s - \mathbf{r}_t|} \, \mathrm{d}^3\mathbf{r}_s - \nabla_t \int_{\partial T} (\mathbf{M}(\mathbf{r}_s) \cdot \mathbf{n}) \frac{1}{|\mathbf{r}_s - \mathbf{r}_t|} \, \mathrm{d}^2\mathbf{r}_s \right] \tag{4.71}$$

And with $\nabla_t \frac{1}{|\mathbf{r}_s - \mathbf{r}_t|} = -\nabla_s \frac{1}{|\mathbf{r}_s - \mathbf{r}_t|}$:

$$\mathbf{H}(\mathbf{r}_t) = \frac{1}{4\pi}\hat{D} \underbrace{\int_T \nabla_s \frac{1}{|\mathbf{r}_s - \mathbf{r}_t|} \, \mathrm{d}^3\mathbf{r}_s}_{\mathbf{H}_T(\mathbf{r}_t)} + \frac{1}{4\pi} \underbrace{\int_{\partial T} (\mathbf{M}(\mathbf{r}_s) \cdot \mathbf{n})\nabla_t \frac{1}{|\mathbf{r}_s - \mathbf{r}_t|} \, \mathrm{d}^2\mathbf{r}_s}_{\mathbf{H}_{\partial T}(\mathbf{r}_t)} \tag{4.72}$$

The volume contribution can be easily calculated (see section 4.3.3) using the surface triangles $\sum_i \Delta_i = \partial T$:

$$\mathbf{H}_T(\mathbf{r}_t) = \int_T \nabla_s \frac{1}{|\mathbf{r}_s - \mathbf{r}_t|} \, \mathrm{d}^3\mathbf{r}_s = \sum_{j=1}^{4} \int_{\Delta_j} \frac{1}{|\mathbf{r}_s - \mathbf{r}_t|} \, \mathrm{d}^2\mathbf{r}_s = -\sum_{j=1}^{4} 4\pi \mathbf{n}_j E_{00}(\Delta_j, \mathbf{r}_s)$$

$$(4.73)$$

For the surface contribution $\mathbf{M}(\mathbf{r}_1) \cdot \mathbf{n}$ from the previous section is used and the surface triangles Δ_i:

$$\mathbf{H}_{\partial T}(\mathbf{r}_t) = \int_{\partial T} (\mathbf{M}(\mathbf{r}_s) \cdot \mathbf{n}) \nabla_t \frac{1}{|\mathbf{r}_s - \mathbf{r}_t|} \, \mathrm{d}^2\mathbf{r}_s \qquad (4.74)$$

$$= \int_{\partial T} (\mathbf{M}(\mathbf{r}_s) \cdot \mathbf{n}) \frac{\mathbf{r}_s - \mathbf{r}_t}{|\mathbf{r}_s - \mathbf{r}_t|^3} \, \mathrm{d}^2\mathbf{r}_s \qquad (4.75)$$

$$= \int_{\partial T} \begin{pmatrix} x_s - x_t \\ y_s - y_t \\ -z_t \end{pmatrix} \frac{m_x x_s + m_y y_s + m_c}{|\mathbf{r}_s - \mathbf{r}_t|^3} \, \mathrm{d}^3\mathbf{r}_s \qquad (4.76)$$

To get rid of $\mathbf{r}_t$ in $\frac{1}{|\mathbf{r}_t - \mathbf{r}_s|}$ the following substitution is made:

$$x_s \to x_s + x_t, \text{ and } y_s \to y_s + y_t, \qquad (4.77)$$

which gives:

$$\mathbf{H}_{\partial T}(\mathbf{r}_t) = \int_{\partial T} \begin{pmatrix} x_s \\ y_s \\ -z_t \end{pmatrix} \frac{m_x(x_s + x_t) + m_y(y_s + y_t) + m_c}{\sqrt{x_s^2 + y_s^2 + z_t^2}} \, \mathrm{d}^3\mathbf{r}_s \qquad (4.78)$$

$$= \sum_{\Delta_i} \frac{4\pi}{z_t} \begin{pmatrix} m_x(x_t D_{10} + D_{20}) + m_y(y_t D_{10} + D_{11}) + m_c D_{10} \\ m_x(x_t D_{01} + D_{11}) + m_y(y_t D_{01} + D_{02}) + m_c D_{01} \\ -z_t m_x(x D_{00} - D_{10}) - z_t m_y(y D_{00} - D_{01}) - z_t m_c D_{00} \end{pmatrix}$$

$$(4.79)$$

4. FMM

4.4. Multipole Expansion

This section describes the three-dimensional Taylor expansion that lies at the heart
of the multipole and local expansions explained in section 4.4.2 and section 4.4.3.
Section 4.4.4 discusses how multipole moments can be reused by shifting expansion
centers. The formulas derived in the next sections are collected for reference in
section 4.4.5.

4.4.1. Taylor Expansion

This section discusses the notation and use of the Taylor expansion. The standard
three-dimensional Taylor expansion of $f(\mathbf{x})$ at $\mathbf{a} \in \mathbb{R}^3$ with the triple index $\mathbf{n} =
(n_1, n_2, n_3)$ in multi-index notation with maximum multipole order P is used:

$$f(\mathbf{x}) \approx \sum_{|\mathbf{n}| \leq P} \frac{(\mathbf{x} - \mathbf{a})^{\mathbf{n}}}{\mathbf{n}!} \left(\partial^{\mathbf{n}} f\right)(\mathbf{a}) \tag{4.80}$$

Expanding $\mathbf{r}_s$ in $\frac{1}{|\mathbf{r}_t - \mathbf{r}_s|}$ around $\mathbf{a} = \mathbf{r}_M$ gives:

$$\frac{1}{|\mathbf{r}_t - \mathbf{r}_s|} = \sum_{|\mathbf{n}| \leq P} \frac{(\mathbf{r}_s - \mathbf{r}_M)^{\mathbf{n}}}{\mathbf{n}!} \left(\partial_s^{\mathbf{n}} \frac{1}{|\mathbf{r}_t - \mathbf{r}_s|}\right)\Bigg|_{\mathbf{r}_s = \mathbf{r}_M} + \mathcal{O}\left(\frac{|\mathbf{r}_s - \mathbf{r}_M|^{P+1}}{|\mathbf{r}_t - \mathbf{r}_s|^{P+2}}\right) \tag{4.81}$$

$$= \sum_{|\mathbf{n}| \leq P} \frac{(\mathbf{r}_s - \mathbf{r}_M)^{\mathbf{n}}}{\mathbf{n}!} \partial_M^{\mathbf{n}} \frac{1}{|\mathbf{r}_t - \mathbf{r}_M|} + \mathcal{O}\left(\frac{|\mathbf{r}_s - \mathbf{r}_M|^{P+1}}{|\mathbf{r}_t - \mathbf{r}_s|^{P+2}}\right) \tag{4.82}$$

$$= \sum_{|\mathbf{n}| \leq P} \frac{(\mathbf{r}_s - \mathbf{r}_M)^{\mathbf{n}}}{\mathbf{n}!} D_{\mathbf{n}}^M(\mathbf{r}_t - \mathbf{r}_M) + \mathcal{O}\left(\frac{|\mathbf{r}_s - \mathbf{r}_M|^{P+1}}{|\mathbf{r}_t - \mathbf{r}_s|^{P+2}}\right) \tag{4.83}$$

$$\approx \sum_{|\mathbf{n}| \leq P} \frac{1}{\mathbf{n}!} (\mathbf{r}_s - \mathbf{r}_M)^{\mathbf{n}} D_{\mathbf{n}}^M(\mathbf{r}_t - \mathbf{r}_M), \tag{4.84}$$

with $\mathbf{n}! = n_x! n_y! n_z!$, $|\mathbf{n}| = n_x + n_y + n_z$ and $\mathbf{r}_t^{\mathbf{n}} = x'^{n_x} y'^{n_y} z'^{n_z}$, the truncation error
$\mathcal{O}\left(\frac{|\mathbf{r}_s - \mathbf{r}_M|^{P+1}}{|\mathbf{r}_t - \mathbf{r}_s|^{P+2}}\right)$, caused by the truncation order P, and the differential function

$$D_{\mathbf{n}}^M(\mathbf{r} - \mathbf{r}_M) = \partial_M^{\mathbf{n}} \frac{1}{|\mathbf{r} - \mathbf{r}_M|}, \tag{4.85}$$
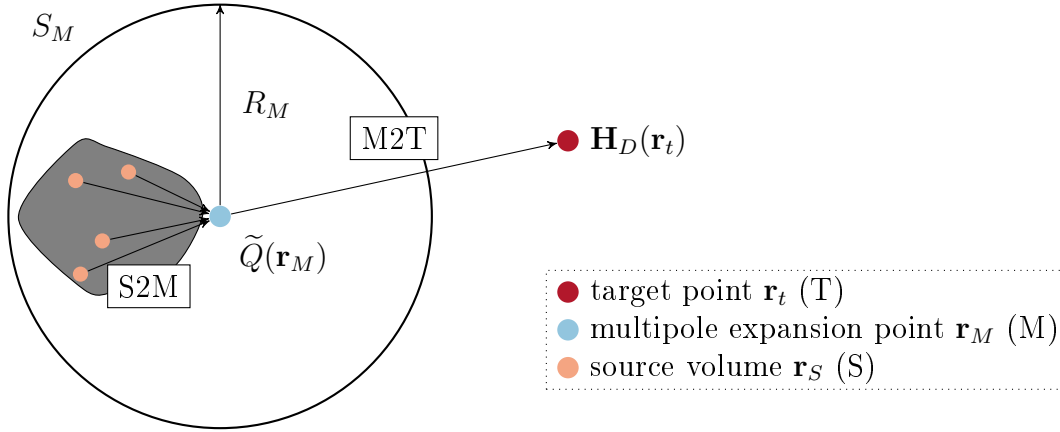
Figure 4.6.: A sketch of the source expansion showing the combination of sources into a multipole moment $\widetilde{Q}(\mathbf{r}_M)$ and the evaluation of the multipole moment at the target $\mathbf{r}_t$ outside of S_M.

where the M in $D_{\mathbf{n}}^M$ indicates the derivative with respect to $\mathbf{r}_M$.

Setting $\mathbf{r}_M = 0$ gives:

$$\frac{1}{|\mathbf{r}_t - \mathbf{r}_s|} \approx \frac{1}{\mathbf{n}!}\mathbf{r}_s^{\mathbf{n}}D_{\mathbf{n}}^t(-\mathbf{r}_t) \tag{4.86}$$

Note that:

$$D_{\mathbf{n}}(-\mathbf{r}) = (-1)^{\mathbf{n}}D_{\mathbf{n}}(\mathbf{r}) \tag{4.87}$$

4.4.2. Source Expansion

The multipole expansion is an approximation of field and potential done by expanding the kernel $\frac{1}{|\mathbf{r}_t-\mathbf{r}_s|}$ as a Taylor series (see 4.4.1) in the far field. The source expansion approximates the magnetization using multipole moments $\widetilde{Q}_{\mathbf{n}}(\mathbf{r}_M)$. Consider a magnetized region Ω with magnetization $\mathbf{M}(\mathbf{r}_s)$ inside a sphere S_M with radius R_M (see figure 4.6). Expansion of field $H_D(\mathbf{r}_t)$ 3.22 and potential $u(\mathbf{r}_t)$ 3.21 around

$\mathbf{r}_M$ give the following results valid outside of S_M:

$$\mathbf{H}_D(\mathbf{r}_t) = -\frac{1}{4\pi}\nabla_t\left(\int_\Omega \mathbf{M}(\mathbf{r}_s)\cdot\nabla_s\left(\frac{1}{|\mathbf{r}_t - \mathbf{r}_s|}\right)\mathrm{d}\mathbf{r}_s\right) \tag{4.88}$$

$$= -\frac{1}{4\pi}\sum_{|\mathbf{n}|\leq p}\nabla_t\int_\Omega \mathbf{M}(\mathbf{r}_s)\cdot\nabla_s\mathbf{r}_{sM}^{\mathbf{n}}D_{\mathbf{n}}^M(\mathbf{r}_t - \mathbf{r}_M)\frac{1}{\mathbf{n}!}\,\mathrm{d}\mathbf{r}_s \tag{4.89}$$

$$= -\frac{1}{4\pi}\sum_{|\mathbf{n}|\leq p}\nabla_t D_{\mathbf{n}}^M(\mathbf{r}_t - \mathbf{r}_M)\frac{1}{\mathbf{n}!}\int_\Omega \mathbf{M}(\mathbf{r}_s)\cdot\nabla_s\mathbf{r}_{sM}^{\mathbf{n}}\,\mathrm{d}\mathbf{r}_s \tag{4.90}$$

$$= -\frac{1}{4\pi}\sum_{|\mathbf{n}|\leq p}\nabla_t D_{\mathbf{n}}^M(\mathbf{r}_t - \mathbf{r}_M)\widetilde{Q}_{\mathbf{n}}(\mathbf{r}_M) \tag{4.91}$$

$$u(\mathbf{r}_t) = \frac{1}{4\pi}\sum_{|\mathbf{n}|\leq p} D_{\mathbf{n}}^M(\mathbf{r}_t - \mathbf{r}_M)\widetilde{Q}_{\mathbf{n}}(\mathbf{r}_M), \tag{4.92}$$

with $\mathbf{r}_{sM} = \mathbf{r}_s - \mathbf{r}_M$,

$$\nabla D_{\mathbf{n}}(\mathbf{r}) = \text{sign}(\mathbf{r})\begin{pmatrix} D_{\mathbf{n}+\hat{\mathbf{x}}}(\mathbf{r}) \\ D_{\mathbf{n}+\hat{\mathbf{y}}}(\mathbf{r}) \\ D_{\mathbf{n}+\hat{\mathbf{z}}}(\mathbf{r}) \end{pmatrix}, \tag{4.93}$$

where

$$\mathbf{n}+\hat{\mathbf{x}} = \begin{pmatrix} n_x + 1 \\ n_y \\ n_z \end{pmatrix}, \; \mathbf{n}+\hat{\mathbf{y}} = \begin{pmatrix} n_x \\ n_y + 1 \\ n_z \end{pmatrix}, \; \mathbf{n}+\hat{\mathbf{z}} = \begin{pmatrix} n_x \\ n_y \\ n_z + 1 \end{pmatrix}, \tag{4.94}$$

and the expansion coefficients (S2M) $\widetilde{Q}_{\mathbf{n}}$, which can be calculated exactly for linearly magnetized tetrahedra using Gaussian quadrature (see 4.4.4), are defined by

$$\widetilde{Q}_{\mathbf{n}}(\mathbf{r}_M) = \frac{1}{\mathbf{n}!}\int_\Omega \mathbf{M}(\mathbf{r}_s)\cdot\nabla_s\mathbf{r}_{sM}^{\mathbf{n}}\,\mathrm{d}\mathbf{r}_s. \tag{4.95}$$

4.4.3. Local Expansion

Another approximation necessary for the FMM is the local expansion. It approximates the field in a target region by introducing a local moment $L_{\mathbf{k}}(\mathbf{r}_L)$ near evaluation points $\mathbf{r}_t$. Consider a source expansion Q valid outside the sphere S_M
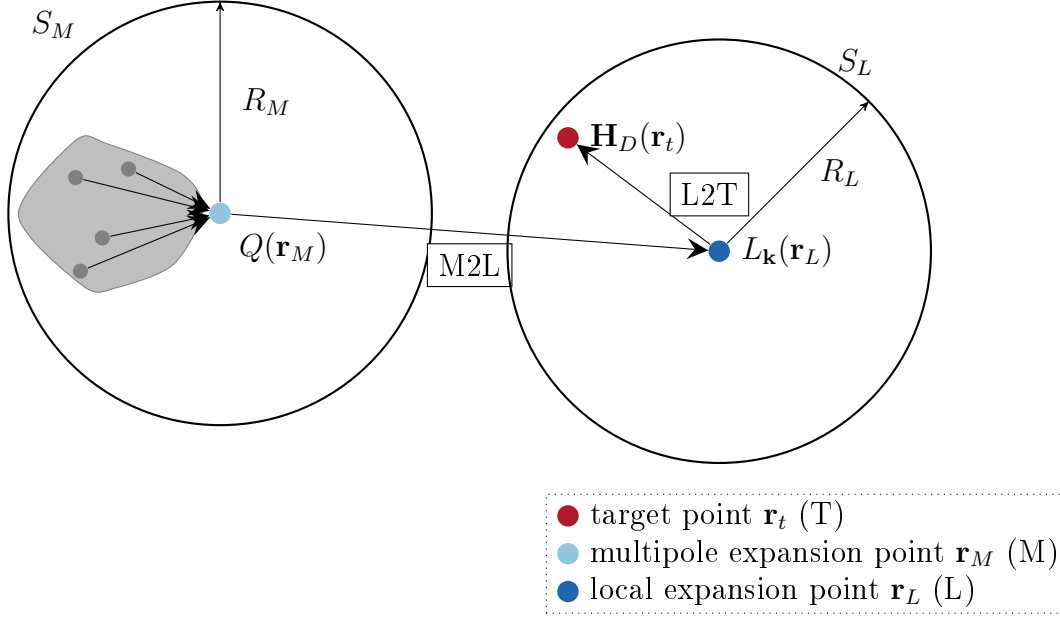
Figure 4.7.: A sketch of the local expansion. It shows the transformation of multipole moment Q to local moment $L_{\mathbf{k}}$ and the evaluation of local moment $L_{\mathbf{k}}(\mathbf{r}_L)$ at target point $\mathbf{r}_t$.

with radius R_M centered at $\mathbf{r}_M \in \mathbb{R}^3$. For a local expansion point $\mathbf{r}_L \in \mathbb{R}^3$ outside of S_M, the kernel $\frac{1}{|\mathbf{r}_t - \mathbf{r}_s|}$ can be written as

$$\frac{1}{|\mathbf{r}_t - \mathbf{r}_s|} = \frac{1}{|(\mathbf{r}_t - \mathbf{r}_L) + (\mathbf{r}_L - \mathbf{r}_M) + (\mathbf{r}_M - \mathbf{r}_s)|} \tag{4.96}$$

$$= \frac{1}{|(\mathbf{r}_{tL}) + (\mathbf{r}_{LM}) + (\mathbf{r}_{Ms})|} \tag{4.97}$$

$$\approx \sum_{|\mathbf{n}| \leq p} \frac{(\mathbf{r}_{ts} - \mathbf{r}_{LM})^{\mathbf{n}}}{\mathbf{n}!} \left(\partial_{ts}^{\mathbf{n}} \frac{1}{|\mathbf{r}_{ts}|} \right) \Big|_{\mathbf{r}_{ts} = \mathbf{r}_{LM}} \tag{4.98}$$

$$\approx \sum_{|\mathbf{n}| \leq p} \frac{(\mathbf{r}_{tL} + \mathbf{r}_{Ms})^{\mathbf{n}}}{\mathbf{n}!} \left(\partial^{\mathbf{n}} \frac{1}{|\mathbf{r}|} \right) \Big|_{\mathbf{r} = \mathbf{r}_{LM}} \tag{4.99}$$

$$\approx \sum_{|\mathbf{n}| \leq p} \frac{(\mathbf{r}_{tL} + \mathbf{r}_{Ms})^{\mathbf{n}}}{\mathbf{n}!} D_{\mathbf{n}}^{LM}(\mathbf{r}_{LM}). \tag{4.100}$$

4. FMM

Using the binomial theorem for

$$(\mathbf{r}_{tL} + \mathbf{r}_{Ms})^{\mathbf{n}} = \sum_{\mathbf{k} \leq \mathbf{n}} \frac{\mathbf{n}!}{(\mathbf{n} - \mathbf{k})!\mathbf{k}!} \mathbf{r}_{tL}^{\mathbf{k}} \mathbf{r}_{Ms}^{\mathbf{n}-\mathbf{k}} \tag{4.101}$$

$$\sum_{|\mathbf{n}| \leq p} \frac{(\mathbf{r}_{tL} + \mathbf{r}_{Ms})^{\mathbf{n}}}{\mathbf{n}!} D_{\mathbf{n}}^{LM}(\mathbf{r}_{LM}) = \tag{4.102}$$

$$\sum_{|\mathbf{n}| \leq p} \sum_{\mathbf{k} \leq \mathbf{n}} \frac{1}{(\mathbf{n} - \mathbf{k})!\mathbf{k}!} \mathbf{r}_{tL}^{\mathbf{k}} \mathbf{r}_{Ms}^{\mathbf{n}-\mathbf{k}} D_{\mathbf{n}}^{LM}(\mathbf{r}_{LM}) \tag{4.103}$$

and some index rearrangement [65] give:

$$\frac{1}{|\mathbf{r}_t - \mathbf{r}_s|} \approx \sum_{|\mathbf{k}| \leq p} \frac{\mathbf{r}_{tL}^{\mathbf{k}}}{\mathbf{k}!} \sum_{|\mathbf{n}| \leq p - |\mathbf{k}|} \frac{\mathbf{r}_{Ms}^{\mathbf{n}}}{\mathbf{n}!} D_{\mathbf{n}+\mathbf{k}}^{LM}(\mathbf{r}_{LM}) \tag{4.104}$$

Similar to section 4.4.2 the expanded kernel is used for the potential and field equations:

$$\mathbf{H}_D(\mathbf{r}_t) = \nabla_t \left(\int_\Omega \mathbf{M}(\mathbf{r}_s) \cdot \nabla_s \left(\frac{1}{|\mathbf{r}_t - \mathbf{r}_s|} \right) \mathrm{d}\mathbf{r}_s \right) \tag{4.105}$$

$$= \nabla_t \left(\sum_{|\mathbf{k}| \leq p} \frac{\mathbf{r}_{tL}^{\mathbf{k}}}{\mathbf{k}!} \sum_{|\mathbf{n}| \leq p - |\mathbf{k}|} D_{\mathbf{n}+\mathbf{k}}^{LM}(\mathbf{r}_{LM}) \frac{1}{\mathbf{n}!} \int_\Omega \mathbf{M}(\mathbf{r}_s) \cdot \nabla_s \mathbf{r}_{Ms}^{\mathbf{n}} \mathrm{d}\mathbf{r}_s \right) \tag{4.106}$$

$$= \nabla_t \left(\sum_{|\mathbf{k}| \leq p} \frac{\mathbf{r}_{tL}^{\mathbf{k}}}{\mathbf{k}!} \sum_{|\mathbf{n}| \leq p - |\mathbf{k}|} D_{\mathbf{n}+\mathbf{k}}^{LM}(\mathbf{r}_{LM}) Q_{\mathbf{n}}(\mathbf{r}_M) \right) \tag{4.107}$$

$$u(\mathbf{r}) = \sum_{|\mathbf{k}| \leq p} \frac{\mathbf{r}_{tL}^{\mathbf{k}}}{\mathbf{k}!} \sum_{|\mathbf{n}| \leq p - |\mathbf{k}|} D_{\mathbf{n}+\mathbf{k}}^{LM}(\mathbf{r}_{LM}) Q_{\mathbf{n}}(\mathbf{r}_M) \tag{4.108}$$

with

$$Q_{\mathbf{n}}(\mathbf{r}_M) = (-1)^{|\mathbf{n}|} \widetilde{Q}_{\mathbf{n}}(\mathbf{r}_M) = \frac{1}{\mathbf{n}!} \int_\Omega \mathbf{M}(\mathbf{r}_s) \cdot \nabla_s \mathbf{r}_{Ms}^{\mathbf{n}} \mathrm{d}\mathbf{r}_s \tag{4.109}$$

$$L_{\mathbf{k}}(\mathbf{r}_L) = \sum_{|\mathbf{n}| \leq p - |\mathbf{k}|} D_{\mathbf{n}+\mathbf{k}}^{LM}(\mathbf{r}_{LM}) Q_{\mathbf{n}}(\mathbf{r}_M) \tag{4.110}$$

$$\mathbf{H}_D(\mathbf{r}_t) = \sum_{|\mathbf{k}| \leq p} \frac{\nabla_t \mathbf{r}_{tL}^{\mathbf{k}}}{\mathbf{k}!} L_{\mathbf{k}}(\mathbf{r}_L). \tag{4.111}$$

4.4.4. Translation of Expansion Centers

The FMM relies on distribution and combination of expansion coefficients at various levels. Expansion coefficients can only be trivially added at a common expansion center. The translation of expansion centers allows just that. Decomposition of $\mathbf{r}_{tL}$ and $\mathbf{r}_{Ms}$ gives an additional level in the FMM tree:

$$\mathbf{r}_{Ms} = \mathbf{r}_{Mm} + \mathbf{r}_{ms} \tag{4.112}$$

$$\mathbf{r}_{tL} = \mathbf{r}_{tl} + \mathbf{r}_{lL}, \tag{4.113}$$

where $\mathbf{r}_L$ and $\mathbf{r}_M$ are intermediate points.

Using the binomial theorem for the multipole moments allows multipole translation from $\mathbf{r}_m$ to $\mathbf{r}_M$.

$$Q_{\mathbf{n}}(\mathbf{r}_M) = \frac{1}{\mathbf{n}!} \int_{\Omega} \mathbf{M}(\mathbf{r}_s) \cdot \nabla_s \mathbf{r}_{Ms}^{\mathbf{n}} \mathrm{d}\mathbf{r}_s \tag{4.114}$$

$$Q_{\mathbf{n}}(\mathbf{r}_M) = \frac{1}{\mathbf{n}!} \int_{\Omega} \mathbf{M}(\mathbf{r}_s) \cdot \nabla_s \left(\mathbf{r}_{Mm} + \mathbf{r}_{ms}\right)^{\mathbf{n}} \mathrm{d}\mathbf{r}_s \tag{4.115}$$

$$Q_{\mathbf{n}}(\mathbf{r}_M) = \frac{1}{\mathbf{n}!} \int_{\Omega} \mathbf{M}(\mathbf{r}_s) \cdot \nabla_s \left(\sum_{\mathbf{k} \leq \mathbf{n}} \frac{\mathbf{n}!}{(\mathbf{n} - \mathbf{k})! \mathbf{k}!} \mathbf{r}_{Mm}^{\mathbf{k}} \mathbf{r}_{ms}^{\mathbf{n}-\mathbf{k}}\right) \mathrm{d}\mathbf{r}_s \tag{4.116}$$

$$Q_{\mathbf{n}}(\mathbf{r}_M) = \frac{1}{\mathbf{n}!} \sum_{\mathbf{k} \leq \mathbf{n}} \frac{\mathbf{n}!}{(\mathbf{n} - \mathbf{k})! \mathbf{k}!} \mathbf{r}_{Mm}^{\mathbf{k}} \int_{\Omega} \mathbf{M}(\mathbf{r}_s) \cdot \nabla_s \mathbf{r}_{ms}^{\mathbf{n}-\mathbf{k}} \mathrm{d}\mathbf{r}_s \tag{4.117}$$

$$Q_{\mathbf{n}}(\mathbf{r}_M) = \sum_{\mathbf{k} \leq \mathbf{n}} \frac{1}{\mathbf{k}!} \mathbf{r}_{Mm}^{\mathbf{k}} \frac{1}{(\mathbf{n} - \mathbf{k})!} \int_{\Omega} \mathbf{M}(\mathbf{r}_s) \cdot \nabla_s \mathbf{r}_{ms}^{\mathbf{n}-\mathbf{k}} \mathrm{d}\mathbf{r}_s \tag{4.118}$$

$$Q_{\mathbf{n}}(\mathbf{r}_M) = \sum_{\mathbf{k} \leq \mathbf{n}} \frac{\mathbf{r}_{Mm}^{\mathbf{k}}}{\mathbf{k}!} Q_{\mathbf{n}-\mathbf{k}}(\mathbf{r}_m) \tag{4.119}$$

A similar derivation for the local moments gives:

$$\mathbf{H}_D(\mathbf{r}_t) = \sum_{|\mathbf{k}| \leq p} \frac{\nabla_t \mathbf{r}_{tL}^{\mathbf{k}}}{\mathbf{k}!} L_{\mathbf{k}}(\mathbf{r}_L) \tag{4.120}$$

$$\mathbf{H}_D(\mathbf{r}_t) = \sum_{|\mathbf{k}| \leq p} \frac{\nabla_t \left(\mathbf{r}_{tl} + \mathbf{r}_{lL}\right)^{\mathbf{k}}}{\mathbf{k}!} L_{\mathbf{k}}(\mathbf{r}_L) \tag{4.121}$$

$$\mathbf{H}_D(\mathbf{r}_t) = \sum_{|\mathbf{k}| \leq p} \frac{1}{\mathbf{k}!} \nabla_t \left(\sum_{\mathbf{l} \leq \mathbf{k}} \frac{\mathbf{k}!}{(\mathbf{k}-\mathbf{l})!\mathbf{l}!} \mathbf{r}_{tl}^{\mathbf{l}} \mathbf{r}_{lL}^{\mathbf{k}-\mathbf{l}} \right) L_{\mathbf{k}}(\mathbf{r}_L) \tag{4.122}$$

$$\mathbf{H}_D(\mathbf{r}_t) = \sum_{|\mathbf{k}| \leq p} \sum_{|\mathbf{l}| \leq p} \frac{\delta_{\mathbf{l} \leq \mathbf{k}}}{(\mathbf{k}-\mathbf{l})!\mathbf{l}!} \nabla_t \mathbf{r}_{tl}^{\mathbf{l}} \mathbf{r}_{lL}^{\mathbf{k}-\mathbf{l}} L_{\mathbf{k}}(\mathbf{r}_L) \tag{4.123}$$

$$\mathbf{H}_D(\mathbf{r}_t) = \sum_{|\mathbf{l}| \leq p} \sum_{\mathbf{k}=\mathbf{l}}^{|\mathbf{k}| \leq p} \frac{1}{(\mathbf{k}-\mathbf{l})!\mathbf{l}!} \nabla_t \mathbf{r}_{tl}^{\mathbf{l}} \mathbf{r}_{lL}^{\mathbf{k}-\mathbf{l}} L_{\mathbf{k}}(\mathbf{r}_L) \tag{4.124}$$

Redefining $\mathbf{k} \to \mathbf{k} + \mathbf{l}$

$$\mathbf{H}_D(\mathbf{r}_t) = \sum_{|\mathbf{l}| \leq p} \sum_{|\mathbf{k}| \leq p - |\mathbf{l}|} \frac{1}{\mathbf{k}!\mathbf{l}!} \nabla_t \mathbf{r}_{tl}^{\mathbf{l}} \mathbf{r}_{lL}^{\mathbf{k}} L_{\mathbf{k}}(\mathbf{r}_L) \tag{4.125}$$

$$\mathbf{H}_D(\mathbf{r}_t) = \sum_{|\mathbf{l}| \leq p} \frac{\nabla_t \mathbf{r}_{tl}^{\mathbf{l}}}{\mathbf{l}!} \sum_{|\mathbf{k}| \leq p - |\mathbf{l}|} \frac{\mathbf{r}_{lL}^{\mathbf{k}}}{\mathbf{k}!} L_{\mathbf{k}}(\mathbf{r}_L) \tag{4.126}$$

gives the new local moment

$$\mathbf{H}_D(\mathbf{r}_t) = \sum_{|\mathbf{l}| \leq p} \frac{\nabla_t \mathbf{r}_{tl}^{\mathbf{l}}}{\mathbf{l}!} L_{\mathbf{l}}(\mathbf{r}_l) \tag{4.127}$$

$$L_{\mathbf{l}}(\mathbf{r}_l) = \sum_{|\mathbf{k}| \leq p - |\mathbf{l}|} \frac{\mathbf{r}_{lL}^{\mathbf{k}}}{\mathbf{k}!} L_{\mathbf{k}+\mathbf{l}}(\mathbf{r}_L), \tag{4.128}$$

allowing the field $\mathbf{H}_D(\mathbf{r}_t)$ to be written as

$$\mathbf{H}_D(\mathbf{r}_t) = \begin{pmatrix} L_{1,0,0}(\mathbf{r}_t) \\ L_{0,1,0}(\mathbf{r}_t) \\ L_{0,0,1}(\mathbf{r}_t) \end{pmatrix} \tag{4.129}$$

and the potential $u(\mathbf{r})$ as

$$u(\mathbf{r}_t) = L_{0,0,0}(\mathbf{r}_t), \tag{4.130}$$

where $L_{\mathbf{n}} = L_{n_x,n_y,n_z}$.

Expansion Coefficents   This section explains how to solve the integration for the multipole moments. The expansion coefficients can be calculated *exactly* for linearly magnetized tetrahedra T using a quadrature rule of order $M = |\mathbf{n}| + 1$ because of the polynomial nature of the integrand (see appendix A):

$$\int_T f(\mathbf{r})\,\mathrm{d}^3 r = |T| \sum_{i=1}^{M} f(\boldsymbol{\lambda}_i) w_i, \tag{4.131}$$

using the volume of the tetrahedron $|T|$ and the quadrature points $\boldsymbol{\lambda}_i$, which are given in barycentric coordinates, with associated weights w_i from [66].

$\mathbf{M}(\lambda_i)$ can be easily calculated from the magnetization at the vertices (see appendix A):

$$\mathbf{M}(\lambda_i) = \sum_{k=1}^{4} \mathbf{M}_k \lambda_{ik}, \tag{4.132}$$

where the index k indicates the vertices of T, $\mathbf{M}_k$ indicates the magnetization at the kth vertex, and λ_{ik} indicates the kth component of the ith quadrature point $\boldsymbol{\lambda}_i$.

The source expansion can be calculated with the following equation:

$$Q_{\mathbf{n}}(\mathbf{r}_M) = \frac{1}{\mathbf{n}!} \int_T \mathbf{M}(\mathbf{r}_s) \cdot \nabla_s \mathbf{r}_{Ms}^{\mathbf{n}} \mathrm{d}\mathbf{r}_s \tag{4.133}$$

$$Q_{\mathbf{n}}(\mathbf{r}_M) = \frac{1}{\mathbf{n}!} |\Omega| \sum_{i=1}^{M} \sum_{k=1}^{4} \lambda_{ik} w_i \mathbf{M}_k \cdot \nabla_s \mathbf{r}_{Ms}^{\mathbf{n}} \tag{4.134}$$

with

$$\nabla_{Ms} \mathbf{r}_{Ms}^{\mathbf{n}} = \begin{pmatrix} n_x x_{Ms}^{n_x-1} y_{Ms}^{n_y} z_{Ms}^{n_z} \\ n_y x_{Ms}^{n_x} y_{Ms}^{n_y-1} z_{Ms}^{n_z} \\ n_z x_{Ms}^{n_x} y_{Ms}^{n_y} z_{Ms}^{n_z-1} \end{pmatrix}. \tag{4.135}$$

4.4.5. Summary

The collected formulas from this section are given here for reference. Source expansion (a.k.a. Source to Multipole: S2M):

$$Q_{\mathbf{n}}(\mathbf{r}_M) = \frac{1}{\mathbf{n}!} \int_\Omega \mathbf{M}(\mathbf{r}_s) \cdot \nabla_s \mathbf{r}_{Ms}^{\mathbf{n}} \mathrm{d}\mathbf{r}_s \qquad (4.136)$$

Translation of source expansion center (a.k.a. Multipole to Multipole: M2M):

$$Q_{\mathbf{n}}(\mathbf{r}_M) = \sum_{\mathbf{k} \leq \mathbf{n}} \frac{\mathbf{r}_{Mm}^{\mathbf{k}}}{\mathbf{k}!} Q_{\mathbf{n}-\mathbf{k}}(\mathbf{r}_m), \qquad (4.137)$$

Calculation of local expansion from source expansion (a.k.a. Multipole to Local: M2L):

$$L_{\mathbf{k}}(\mathbf{r}_L) = \sum_{|\mathbf{n}| \leq p - |\mathbf{k}|} D_{\mathbf{n}+\mathbf{k}}^{LM}(\mathbf{r}_{LM}) Q_{\mathbf{n}}(\mathbf{r}_M) \qquad (4.138)$$

Translation of local expansion center (a.k.a. Local to Local: L2L):

$$L_{\mathbf{k}}(\mathbf{r}_L) = \sum_{|\mathbf{n}| \leq p - |\mathbf{k}|} D_{\mathbf{n}+\mathbf{k}}^{LM}(\mathbf{r}_{LM}) Q_{\mathbf{n}}(\mathbf{r}_M) \qquad (4.139)$$

Calculation of field or potential from local expansion (a.k.a. Local to Target: L2T):

$$\mathbf{H}_D(\mathbf{r}_t) = \begin{pmatrix} L_{1,0,0}(\mathbf{r}_t) \\ L_{0,1,0}(\mathbf{r}_t) \\ L_{0,0,1}(\mathbf{r}_t) \end{pmatrix} \qquad (4.140)$$

$$u(\mathbf{r}_t) = L_{0,0,0}(\mathbf{r}_t) \qquad (4.141)$$

Calculation of field or potential from multipole expansion (a.k.a. Multipole To Target: M2T):

$$\mathbf{H}_D(\mathbf{r}_t) = -\frac{1}{4\pi} \sum_{|\mathbf{n}| \leq p} \nabla_t D_{\mathbf{n}}^M(\mathbf{r}_t - \mathbf{r}_M) \widetilde{Q}_{\mathbf{n}}(\mathbf{r}_M) \qquad (4.142)$$
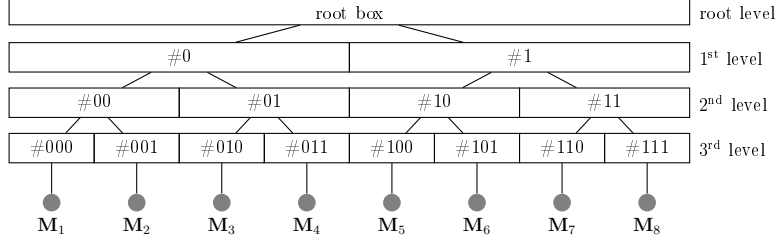
Figure 4.8.: An example of a binary tree spanning a one-dimensional array of point dipole sources $\mathbf{M}_i$ with its tree nodes.

$$u(\mathbf{r}_t) = \frac{1}{4\pi} \sum_{|\mathbf{n}| \leq p} D_{\mathbf{n}}^M(\mathbf{r}_t - \mathbf{r}_M)\widetilde{Q}_{\mathbf{n}}(\mathbf{r}_M), \qquad (4.143)$$

with

$$\widetilde{Q}_{\mathbf{n}}(\mathbf{r}_M) = (-1)^{|\mathbf{n}|}Q_{\mathbf{n}}(\mathbf{r}_M). \qquad (4.144)$$

4.5. One Dimensional $N\log(N)$ Algorithm

This section discusses a simplified version of the FMM to reduce the complexity of the explanation. To avoid confusion, note the difference between discretization cells and octree nodes (i.e., boxes). Discretization cells describe the discretization of space in terms of the finite element method, octree nodes divide the space for applying the FMM algorithm.

Imagine a string consisting of point-like dipoles $\mathbf{M}_i$ with a constant distance between each other (see figure 4.8). First, a root box spanning the whole problem domain is constructed. The root box is then successively split in half until each box contains exactly one source.

Two boxes on the same level can either be neighbors or well-separated. Two boxes are called neighbors if they share a common edge (see figure 4.9 and figure 4.10). The box itself is also considered its own neighbor. To save computation time higher box levels (i.e., larger geometric regions) for computing the interaction are used at larger distances.
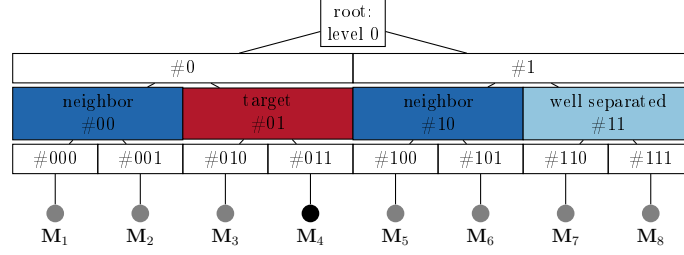
Figure 4.9.: Interaction of the simplified algorithm at level 2. Box 01 uses the multipole moments of well-separated box 11. Interactions for boxes 00 and 10 are continued at a finer tree level (see figure 4.10).

The tree traversal for the simplified algorithm starts at the root. It uses multipole expansion (see section 4.4.2) to calculate the interaction between well-separated boxes. Neighboring boxes are handled differently. The algorithm moves down the tree in a recursive manner using multipole expansion for the well-separated child boxes at a finer level until the algorithm arrives at the leaf (finest) level where the interaction is calculated directly between the leaves' sources.

As an example, consider you want to calculate the interaction list for $\mathbf{M}_4$ in figures 4.8 to 4.10. As mentioned before there are no well-separated boxes at level 1. Thus we start with box 01 at level 2 as depicted in figure 4.9. For the well-separated box 11 the source expansion is used to compute its contribution to the children of the target cell 01. All other boxes are subdivided for further processing. In the next step, we arrive at the 3rd level. The well-separated cells are again computed using their source expansion. Lastly, the remaining neighbors' contributions are calculated directly since they have no children left for applying the recursive algorithm.

The scaling properties are split up as follows:

- The work required at every level is $3Np$ when using P as multipole truncation order and $p = P(P - 1)(P - 2)/6$.
  - Every particle has maximally three next neighbors including itself.
  - The neighboring cells lead to $3 \cdot 2 = 6$ child cells.
  - Subtracting three next neighbor cells because they will be accounted for in the next step gives the computed $6 - 3 = 3$ cells per level.
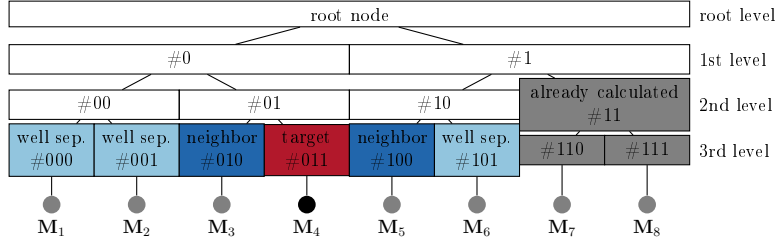
Figure 4.10.: Interaction of the simplified algorithm at level 3. Box 011 uses the multipole moments of well-separated boxes 000, 001 and 101. Interaction with boxes 100 and 010 can only be calculated directly via integration.

- A binary tree has $\log(N)$ levels for the well-balanced case.
- At the leaf level 3 operations including the self-interaction have to be done.

Adding the contributions gives a total of $3NP\log(N)+3N = \mathcal{O}(N\log(N))$ operations. The corresponding number for the two-dimensional case is $28NP^2\log(N)+9N$ and for the three-dimensional case $189NP^3\log(N)+27N$.

For an inhomogeneous source distribution the number of levels cannot be guaranteed. Assuming empty nodes are deleted for practical purposes it remains $\mathcal{O}(\log(N))$, leaving the scaling properties unchanged.

4.6. FMM

This section builds upon the knowledge of the previous section, it describes the changes necessary to reach the promised linear $\mathcal{O}(N)$ scaling and continuous source distribution, namely

- local expansion (=M2L, see section 4.4.3) for approximating the solution in a region near the target,
- translation of expansion centers (=M2M and L2L, see section 4.4.4)
  - for combining source expansions from child boxes
  - and distributing local expansions to child boxes,
- and the discretization of the continuous problem (see section 4.2).

4. FMM

4.6.1. Overview

The algorithm goes through the following steps which are explained in detail in the following sections. An overview is shown in figure 4.11:

Tree Creation The process of dissecting the problem into geometrical cubes in a hierarchical structure.

Upward Pass Creation of multipole moments from sources (Source to Multipole: S2M) and joining of multipole moments into larger geometric regions (Multipole to Multipole: M2M).

Dual-Tree Traversal The dual-tree traversal decides which regions use multipole to local conversion (M2L), and which regions use direct near-field (P2P) interaction on every tree level.

Downward Pass Distribution of local expansions (L2L) and evaluation of local expansions at target points (L2P).

Near-Field Calculation Direct evaluation (P2P) of the source magnetization at the evaluation points.

4.6.2. Tree Creation

Assuming a three-dimensional problem instead of a binary tree, the problem space is recursively divided into smaller cubes. The resulting tree is called an *octree* (see figure 4.12). Two trees are created, one containing all the sources and one containing all the target (i.e., evaluation) points. Each box has a radius R_b containing all discretization cells with at least one discretization node inside the box (see figure 4.13) which will be used to separate near- and far-field solutions.
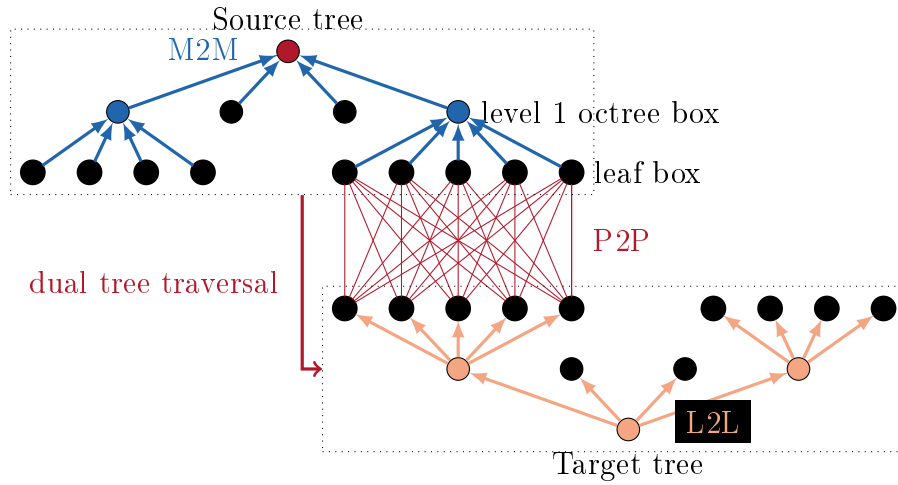
Figure 4.11.: A flow diagram outlining the FMM method. Showing upward pass (M2M), downward pass (L2L) and the overall structure of the algorithm. The decision tree for the dual-tree traversal is explained in section 4.6.4.
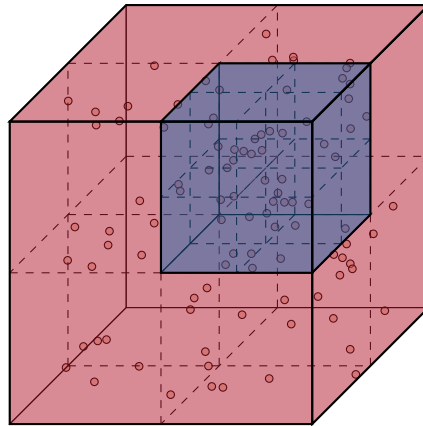

Figure 4.12.: Recursive space division using an octree. First, a box spanning all sources is constructed (red box). The box is recursively split into eight smaller boxes on each level (one is highlighted in blue), until each box contains at most N_p particles.
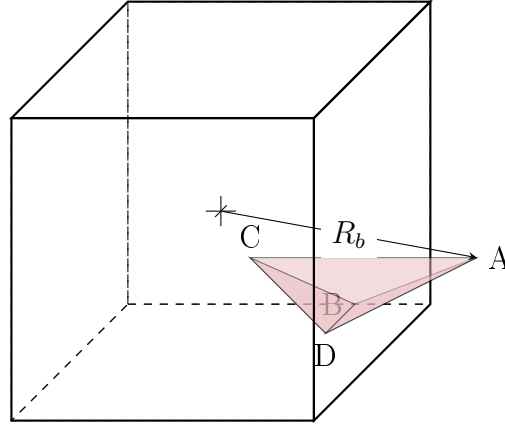
Figure 4.13.: The box radius R_b is defined in a way that it contains all discretization cells with at least one vertex inside the octree box.

4.6.3. Upward Pass

The FMM algorithm starts at the leaf level of the source tree by computing the source expansions at the leaf box centers for each contained source node. The process combines surface and volume terms of the source magnetization inside the node (P2M).

The "actual" upward pass recursively combines the source moments at the parent cell centers by translation (M2M) until it reaches the root (i.e., top) of the octree.

This step has linear scaling which can be seen by considering an octree. The tree has $8^{\log_8 N + 1} = N$ boxes with one set of expansion coefficients ($\propto P^3$) for each box, leading to a complexity of $\mathcal{O}\left((N+1)P^3\right)$.

4.6.4. Dual-Tree Traversal

The traversal strategy for deciding which cells interact at which level is described by figure 4.14. It starts with the initial step, creating octrees for the target and source spaces and then putting the pair of both root boxes on a stack.

The recursive step can be done in parallel for all available stack entries. A thread pops the top-most stack entry. The larger tree in the popped pair is split into its
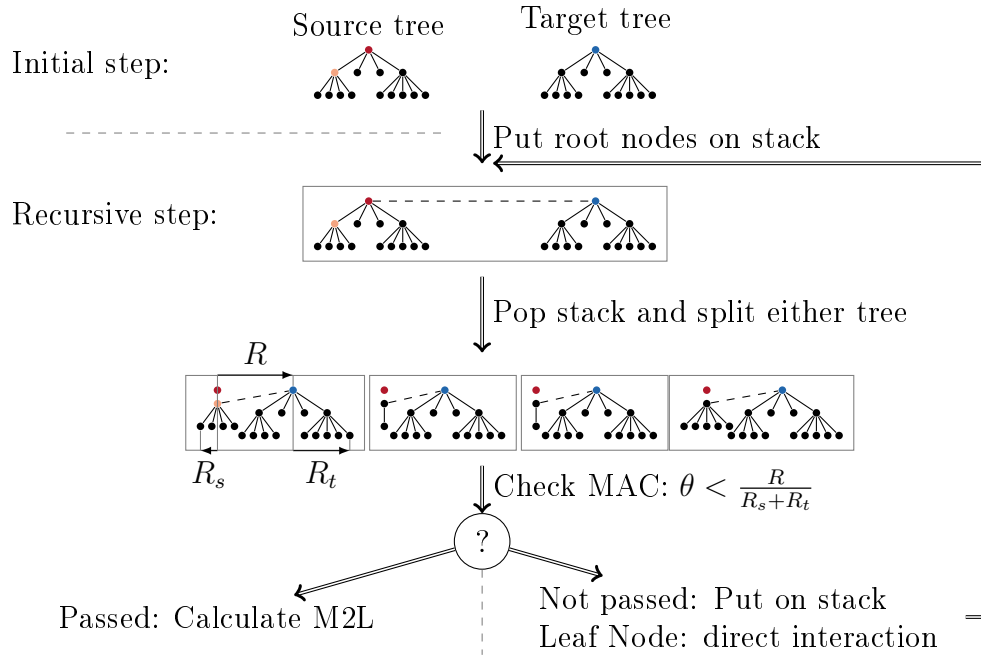
Figure 4.14.: A flow diagram of the dual-tree traversal, showing the initial and first recursive step for a small example tree. The initial step simply creates the tree and puts the root nodes on the stack. The recursive step decides what to do with the stack entries; either calculating the interaction or creating more stack entries on a finer discretization. R is the distance between the source and target tree cell. R_s and R_t stand for the radius of the source and the target cell.

4. FMM

children, giving at most eight new trees at each step. Afterwards, the multipole
acceptance criterion [MAC] is applied to all the newly created children. All the
children that are not fulfilling the MAC are used to create pairs of source and
target tree nodes for the next finer level, and are pushed to the stack; otherwise
(for children fulfilling the MAC), the interaction between source and target tree
is calculated either by local expansion (M2L see section 4.4.3) or—at the leaf
level—by direct integration (P2P see section 4.3).

The method and pseudocode for the recursive step is reprinted from [67] in list-
ing 4.1 and listing 4.2.

<div align="center">Listing 4.1: EvaluateDualTreecode()</div>

```
push pair of root cells (A,B) to stack
while stack is not empty do
  pop stack to get (A,B)
  if target cell is larger then source cell then
    for all children a of target cell A do
      Interact{(a,B)}
    end for
  else
    for all children b of source cell B do
      Interact{(A,b)}
    end for
  end if
end while
```

74

Listing 4.2: Interact(A,B)

```
if A and B are both leaves then
  call P2P kernel
else
  if A and B satisfy MAC then
    call M2L kernel
  else
    push pair (A,B) to stack
  end if
end if
```

To examine the number of evaluation steps, consider the interaction list. It contains at most a set number of boxes proportional to θ^{-3}. The contribution of the dual-tree traversal is proportional to $\mathcal{O}\left(N\left(\frac{P}{\theta}\right)^3\right)$.

4.6.5. Downward Pass

The remaining step evaluates the local moments at the leaves (L2L) and uses the leaf moments to calculate the moments at the targets (L2P). Starting at the root, the local moments are distributed to every child box recursively by translation (L2L see section 4.4.4).

The complexity of this step is analogous to the upward pass complexity. The tree has $8^{\log_8 N + 1} = N$ boxes with one expansion for each box, leading to a complexity of $(N+1)P^3$.

4.6.6. Near-Field Contributions

The near-field contributions (P2P) are calculated by direct integration (see section 4.3). The interactions are stored in matrices for faster subsequent evaluation.

4.7. FEM/FMM

Instead of calculating the whole problem, FMM can also be used in conjunction with the finite element method, by merely calculating the potential at the boundaries and using it as a Dirichlet boundary condition for the FEM code. This method saves near-field calculation time for the FMM by reducing the target evaluation points, and it creates a smooth FEM solution (see [68]) in the volume. The finite element solution is solved by the weak formulation of the Poisson equation:

$$\int_\Omega \nabla \Phi \cdot \nabla \nu \, \mathrm{d}^3 \mathbf{r} = \int_\Omega \mathbf{M} \cdot \nabla \nu \, \mathrm{d}^3 \mathbf{r} \qquad \qquad \forall \nu \in \mathcal{V} \qquad (4.145)$$

The trial space contains the Dirichlet boundary condition as an *essential boundary condition* with $\Phi \in \mathcal{V}$ with $\Phi(\mathbf{r}) = u_{\mathrm{FMM}}(\mathbf{r})$ for $\mathbf{r} \in \partial\Omega$, where $u_{\mathrm{FMM}} = u(\mathbf{r})$ is the FMM solution of the potential on the boundary.

5. Documentation

The following sections are directly imported from the source documentation. They include the main page of the documentation and the most important classes for the user of the library with collaboration diagrams showing their connection to other classes. This section should be seen as an introduction to using, understanding, and extending the source code.

5.1. Main Page

microfmm is an implementation of the Fast Multipole Method supporting MPI and OpenMP. It can either be used as a stand-alone code or interfaced via docker.

The project is split into three directories:

- fmm
- libstrayfield
- python

The fmm directory contains modified and simplified code from `exafmm` to suit the needs of micromagnetic calculations.

The libstrayfield directory is the heart of source containing the implementation of the main implementation, MeshData, NearField, parallelization, and the FMMFactory class for instantiating a class calculating the field or potential.

The python directory contains an interface for `fenics` which uses `numpy` arrays. The interface uses `SWIG` and is implemented in the strayfield.i file.

To build the program the following libraries are needed:

- an MPI library (e.g. `Open MPI`)
- an OpenMP compatible compiler
- `Boost`
- optional: `fenics` for the python and FEM interface

To compile and run the test suite, execute the following commands in bash:

```
mkdir build
cd build
CXX=mpicxx cmake ..
make test_strayfield
cd ..
./build/test/test_strayfield
```

The program should automatically locate the necessary libraries via `CMake`.

A simple documented example program using MPI is given in mpi_cubes.cxx.

Overview of the implementation

The struct AbstractFMM provides the ability to calculate the Potential or Field objects for a problem defined by using MeshData. The actual implementation is done in StrayfieldFMM. The class structure for StrayfieldFMM shows an overview in form of a collaboration diagram including all the important classes. All classes containing the string Abstract or Base in their name are used to improve compilation times and decouple the AbstractFMM in strayfield.h from the StrayfieldFMM implementation in strayfield_impl.h by using FMMFactory. The high-level algorithm is implemented in StrayfieldFMM::calculate where an outline is printed below:

```
using StrayfieldBase::data;
TreeCalc<O, Kind> calc; // creates the octree and interaction lists
Expansion<O> expansion; // calculates the expansion coefficients
const bool mpi;
Kind calculate(){ // calculates the Field or Potential
  calc.near->calculate_matrix(data, calc.targetCells); // calculate near field matrix
```

```
#pragma omp parallel
    {
      // calculate moments for local bodies
      expansion.calculate_moments(calc.sourceBs, calc.divMParts);
      // calculate moments for local octree cells
      upwardPass<O>(calc.sourceCells);
      if(mpi){
#pragma omp barrier
#pragma omp single
        // receive remote magnetization and octree cell moments
        alltoallMagnetization(O, calc.cd_set, calc.buf, *data, *data, calc.remoteOrphanCells);
        //calculate moments for remote bodies
        expansion.calculate_moments(calc.remoteBs, calc.remoteDivMParts);
        // calculate moments for local octree cells
        upwardPass<O>(calc.remoteTree);
      }
#pragma omp barrier
      // calculate multipole to local
      expansion.evaluate_m2l(calc.m2l_list);
      // calculate near-field
      calc.near->evaluate_p2p(data->m, calc.p2p_cells);
#pragma omp barrier
      // calculate field from local moments
      downwardPass<O>(calc.targetCells);
    }
    // map bodies to Field or Potential
    return calc.calculate();
  }
}
```

5.2. StrayfieldFMM< O, Kind > Class Template Reference

StrayfieldFMM< O, Kind > is the main class implementing the Fast Multipole Method.
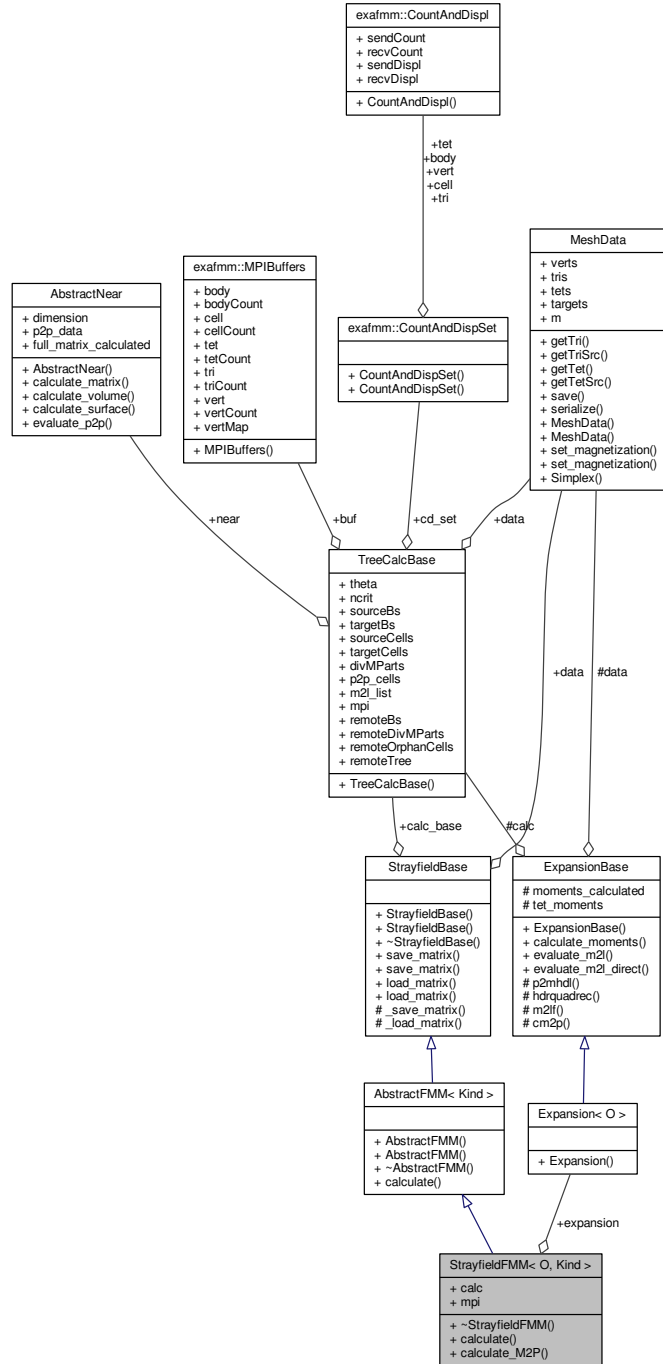
#include <strayfield_impl.h>

Figure 5.1.: Collaboration diagram for StrayfieldFMM< O, Kind >.

Public Member Functions

- Kind calculate ()

  calculates the Field or Potential depending on template argument Kind.
- Kind calculate_M2P ()

  calculates the field or potential without using the local tree.

Public Attributes

- TreeCalc< O, Kind > calc

  creates the octree and multipole interaction lists TreeCalc::m2l_ list.
- Expansion< O > expansion

  calculates the moments for sources and evaluates multipole to local interaction using TreeCalcBase::m2l_ list.
- const bool mpi

  declares whether this class uses MPI parallelization.
- MeshData ∗ data

  provides access to the underlying MeshData containing the vertices, tetrahedra, and triangles of the mesh and their magnetization.
- TreeCalcBase ∗ calc_base

  points to the TreeCalc data structure without the need to use templated classes.

Friends

- class FMMFactory

  creates StrayfieldFMM instances in the form of AbstractFMM∗.

5.2.1. Detailed Description

StrayfieldFMM< O, Kind > is the main class implementing the Fast Multipole Method.

This class should be constructed via FMMFactory.

To understand the FMM source code, it would be wise look at its collaboration diagram (figure 5.1). Starting at the bottom with StrayfieldFMM it has two template arguments: **Kind** describing whether it should calculate Field or Potential and **O** defining the maximum multipole order. It has a templated public function for calculating either Field or Potential passed via the template argument Kind, returning either a vector of vec3 or a vector of scalars. The calculate function implements the main functionality and is reprinted in the main section of the documentation.

5.2.2. Member Data Documentation

calc_base `template<int O, class Kind = Field>`

`TreeCalcBase* StrayfieldBase::calc_base`

points to the TreeCalc data structure without the need to use templated classes.

data `template<int O, class Kind = Field>`

`MeshData* StrayfieldBase::data`

provides access to the underlying MeshData containing the vertices, tetrahedra, and triangles of the mesh and their magnetization.

The documentation for this class was generated from the following file:

- libstrayfield/strayfield_impl.h

5.3. MeshData Struct Reference

MeshData stores data of a tetrahedral mesh and provides access to its triangles, tetrahedra, and their magnetization.

`#include <mesh_data.h>`
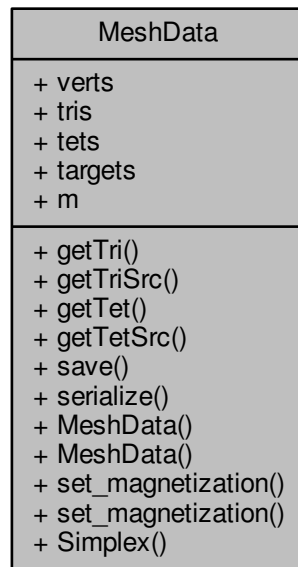

MeshData
+ verts + tris + tets + targets + m
+ getTri() + getTriSrc() + getTet() + getTetSrc() + save() + serialize() + MeshData() + MeshData() + set_magnetization() + set_magnetization() + Simplex()

Figure 5.2.: Collaboration diagram for MeshData.

Public Member Functions

- Stri getTri (const int n) const
  returns the coordinates of the nth triangle.
- Stri getTriSrc (const int n) const
  returns the magnetization of the nth triangle.

- Stet getTet (const int n) const
  returns the coordinates of the nth tetrahedron.
- Stet getTetSrc (const int n) const
  returns the magnetization of the nth tetrahedron.
- void save (const string &filename) const
  saves the current MeshData.
- template<class Archive >
  void **serialize** (Archive &archive)
- MeshData (const string &filename)
  loads data from a file generated with MeshData::save.
- void set_magnetization (const int Nm, const double ∗mx, const double ∗my, const double ∗mz)
  sets the magnetization of the mesh from three arrays.
- void set_magnetization (const int Nm, const double ∗m)
  sets the magnetization of the mesh from one array containing all three components.

Static Public Member Functions

- static MeshData Simplex ()
  returns the most basic MeshData (a Simplex).

Public Attributes

- vector< vec3 > verts
  coordinates of the vertices
- vector< TriIds > tris
  indices of the triangles
- vector< TetIds > tets
  indices of the tetrahedra
- vector< vec3 > targets
  coordinates of the targets
- vector< vec3 > m
  magnetization of the vertices

5.3.1. Constructor & Destructor Documentation

MeshData() `MeshData::MeshData (`

`const string & ` *filename* ` ) [explicit]`

loads data from a file generated with MeshData::save.

An example on how to import data from MPI is given in create_mpi_data.py.

5.3.2. Member Function Documentation

save() `void MeshData::save (`

`const string & ` *filename* ` ) const`

saves the current MeshData. Attention: it cannot be used with MPI yet.

The documentation for this struct was generated from the following files:

- libstrayfield/mesh_data.h
- libstrayfield/mesh_data.cpp

6. Results

The first two subsections of the results section establish the correctness of the near-field and far-field components of the simulation. Section 6.3 shows the shared memory performance in a *weak scaling* scenario and compares the performance to a state of the art hybrid FEM/BEM implementation. The last subsection shows the *strong-scaling* properties of the distributed (MPI) implementation on a multi-node environment using the Vienna Scientific Cluster [VSC].

6.1. Discretization and Near-Field Error

This section establishes the correctness of the near-field algorithm for calculating linearly magnetized tetrahedra (see section 4.3).

To test the correctness of the tetrahedral integrals, the results are checked by comparing randomly generated tetrahedra with randomly generated evaluation points to a reference solution. The reference solutions are obtained by numerical integration using Mathematica's numerical integration routines. These tests are implemented as unit tests in the files `strayfield_test.cpp` and `potential_test.cpp` and reach a relative accuracy of near machine precision.

To analyze the discretization error and the correctness of meshes of tetrahedra two geometries with known analytical solutions are used, namely a homogeneously magnetized sphere [69] and a homogeneously magnetized cube. Both geometries were magnetized with $M_x = M_y = 0$; $M_z = 1$. Figures 6.1 and 6.2 show the results for sphere and cube respectively. The Euclidean norm $L^2((\mathbf{H} - \mathbf{H}_{\text{ref}})/\mathbf{H}_{\text{ref}})$ is used to measure the discretization error, where $\mathbf{H}_{\text{ref}}$ is the analytical solution of the
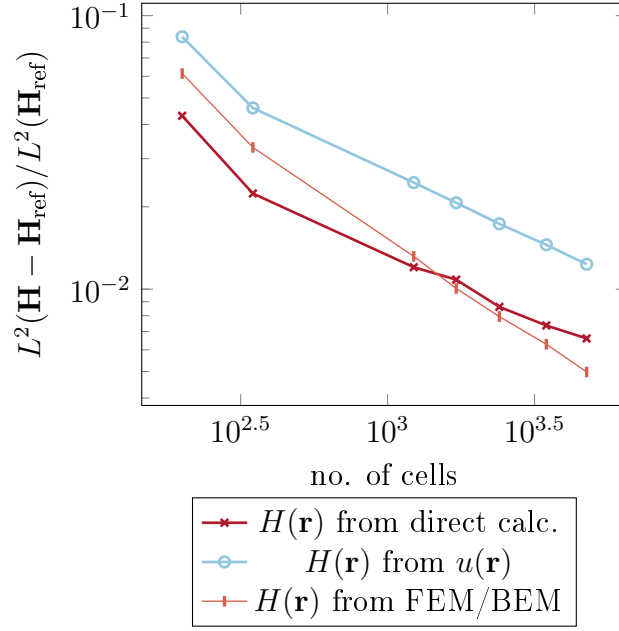
Figure 6.1.: $L^2((\mathbf{H} - \mathbf{H}_{\text{ref}})/\mathbf{H}_{\text{ref}})$ error on a homogeneously magnetized $\mathbf{M} = (0, 0, 1)^T$ sphere mesh for direct calculation of field (i.e., discretization error), via discretized potential, or using a FEM/BEM simulation. $\mathbf{H}_{\text{ref}}$ is the analytic solution of the ideal (i.e., not discretized) sphere. The $\mathbf{H}$ field is evaluated at the cell centers, and the potential u is converted to $\mathbf{H}$ by cell-wise integration [70].

problem. The potential is differentiated cell-wise for comparison with the field $\mathbf{H}$ [70], giving a cell-wise constant field.

Figure 6.1 shows the discretization error of a homogeneously magnetized sphere. It displays a decreasing error with an increasing number of degrees of freedom [DOF]. Furthermore, it allows a comparison of the various near-field implementations, namely direct field, direct potential, and finite element solution. The error might seem large, but figure 6.3 shows that the energy error is small enough for micromagnetic simulations.

Analogously, figure 6.2 shows the field of a homogeneously magnetized cube. The direct field error is omitted because the solution is at machine precision for the given problem.
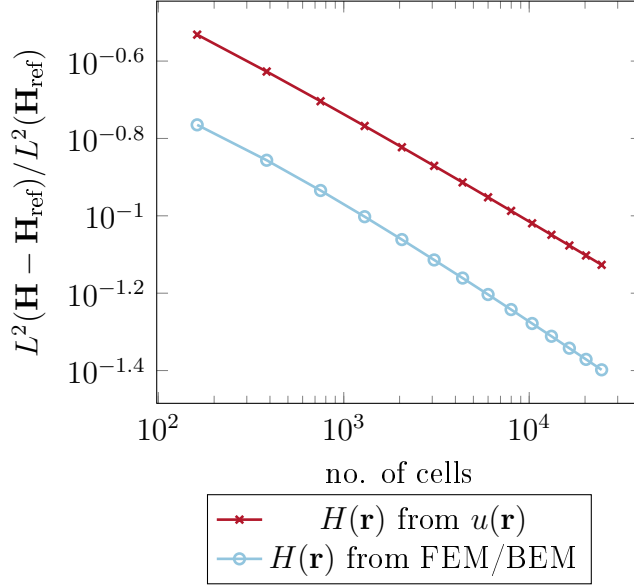
Figure 6.2.: $L^2(\mathbf{H} - \mathbf{H}_{\text{ref}})/L^2(\mathbf{H}_{\text{ref}})$, error on a cube (constant magnetization in z-direction $M_z = 1$) for discretized calculation of field, via potential and FEM/BEM simulation. $\mathbf{H}_{\text{ref}}$ is the analytic solution of the cube [69, 70]. The $\mathbf{H}$ field is evaluated at the cell centers.

To further check the correctness of the near-field code the micromagnetic standard problem 4 [71] is solved using only the near-field solution. The standard problem 4 proposes two switching fields; only switching field 1 is used in figure 6.3. The initial relaxed state is calculated with FEM/BEM using magnum.fe [72], providing an identical starting point for all simulations. The mesh is created using Dolfin's [73] *BoxMesh* with a box size of $(100, 25, 1)$. Both direct-potential and direct-field solution display correct switching behavior as can be seen in figure 6.3 [70]. Time integration is done using a preconditioned time integration method [74].

6.2. Multipole-Expansion Error

Figure 6.4 shows the trade-off that has to be done between solve time and maximum error with varying multipole order P. The method for obtaining the error is taking the maximum error of a the potential evaluation on each vertex of a randomly magnetized cube with saturation magnetization $M_S = 1\,\text{A}\,\text{m}^{-1}$, 134 vertices,
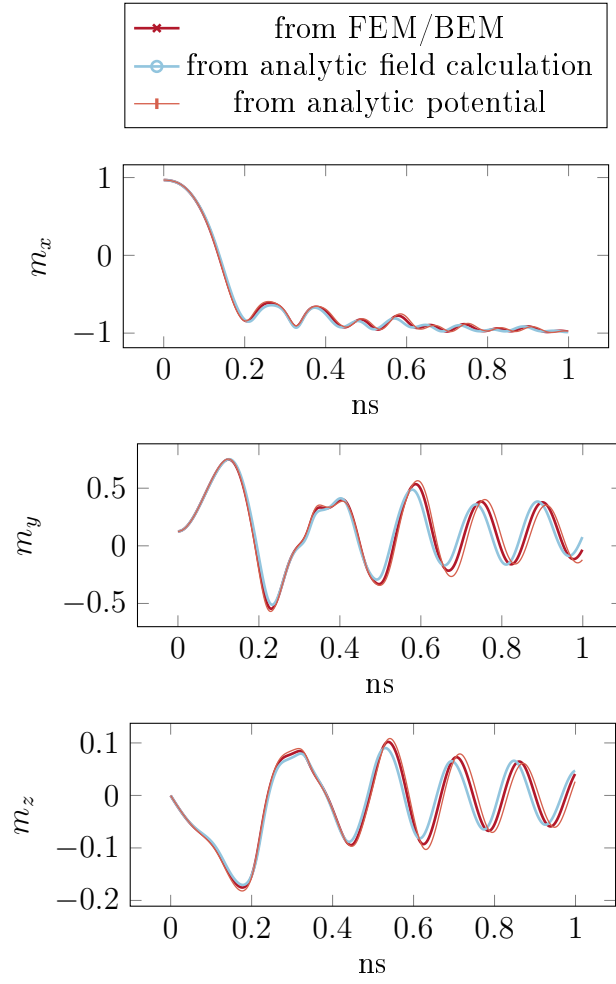
Figure 6.3.: Comparison of the magnetization in x-, y-, and z-direction for the standard problem 4 with *switching field* 1 [71] using a higher order preconditioned BDF scheme [74] for time integration.
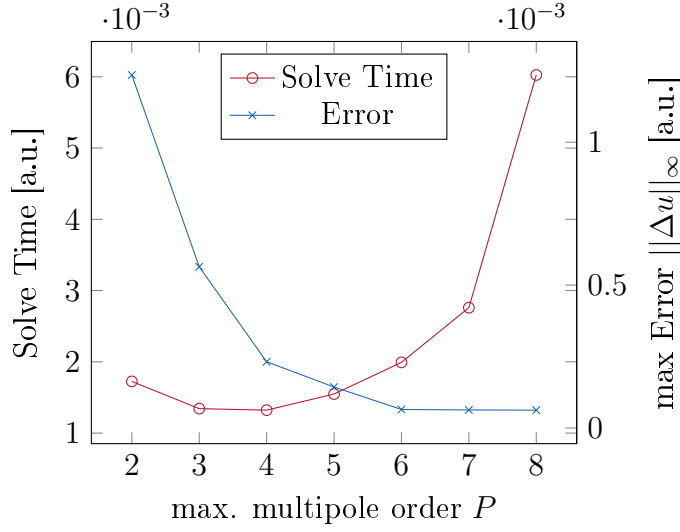
Figure 6.4.: Comparison between error, solve time and mulitpole order P of a randomly magnetized cube of 134 vertices.

and a MAC of $\theta = 0.7$. The reference solution is calculated by solely applying the near-field solution. The error displays the expected θ^P proportionality, and the solve time and storage space of multipole evaluations increase with $\propto P^3$. This test is a strong indicator that the expansions are implemented correctly.

6.3. FMM Shared Memory Performance

Shared memory (OpenMP) parallelizes code on one compute node, i.e., all CPUs can access the same physical memory (RAM). Shared memory enables parallelization with minor modifications to serial code, but is limited in the number of CPUs that can be used.

This section shows the weak scaling (i.e., fixed problem size) performance on a single shared memory machine with up to 16 cores and a comparison of a hybrid FEM/BEM code using a conjugate gradient solver with an algebraic multigrid preconditioner to the presented hybrid FEM/FMM solver (see section 4.7).
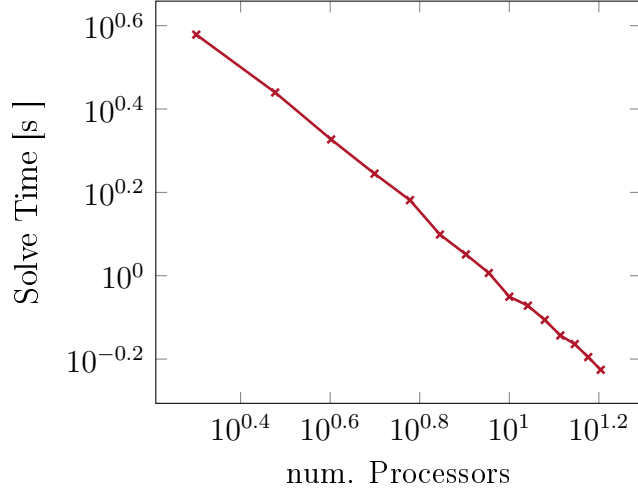
Figure 6.5.: This figure shows the decreasing solve time of a cube with constant
magnetization using an increasing number of cores (1-16). The simu-
lation shows near-perfect weak-scaling properties.

Figure 6.5 shows the near-optimal scaling properties of the stray-field problem. It
calculates a field evaluation after initialization for 357,911 vertices with the pa-
rameters MAC $\theta = 0.3$ and maximum multipole order $P = 4$ on a homogeneously
magnetized cube with up to 16 cores. The simulations are done on a shared mem-
ory machine using two Intel Xeon E5-2650v2 2.6 GHz processors with eight cores
each.

Figure 6.6 compares potential evaluation performance of two algorithms for in-
creasingly larger homogeneously magnetized box meshes. FEM/FMM is the hybrid
algorithm described in section 4.7. The FMM parameters used in the simulation
are multipole acceptance criterion $\theta = 0.5$ and maximum multipole order $P = 3$.
FEM/BEM is a state of the art finite element implementation using a conjugate
gradient solver with an algebraic multigrid preconditioner [75]. Both simulations
are done using the same machine as above and called using a python interface for
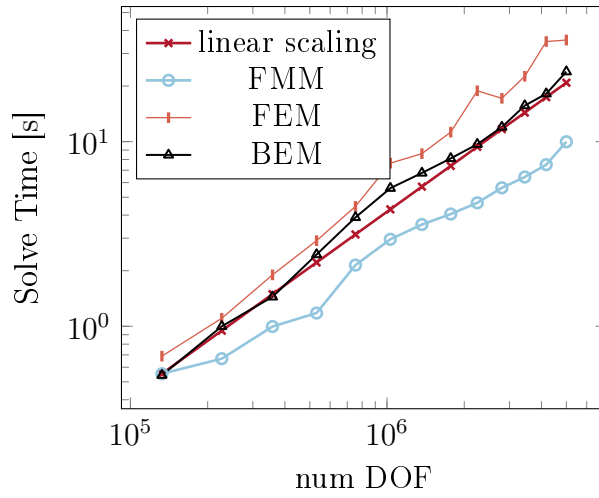comparability.

Figure 6.6.: This figure shows the solve time of FEM, BEM, and FMM with increasing degrees of freedom [DOF] compared to a linear increase in run time. The FEM simulation needs to be done in both cases. The BEM simulation includes the solution of a second FEM problem for the inhomogeneous solution.
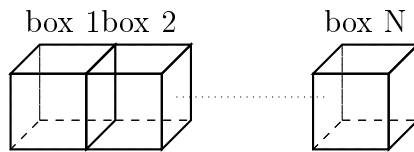

Figure 6.7.: The geometry used for the MPI test is a series of cubes arranged next to each other. Each cube is stored on a separate MPI rank.

6.4. Distributed Performance

The distributed programming model shares data by passing messages. Each thread needs to receive a copy of the necessary data by using the Message Passing Interface [MPI]. Distributed software is slower and more difficult to manage than shared memory software but allows many more CPUs to work in parallel.

This section shows preliminary results using a large number of CPUs with MPI. The implementation shows promising performance and is a working prototype that can be expanded into a production-ready many-core software. The results show the strong-scaling performance for calculating the field of a series of homogeneously magnetized cubes positioned next to each other as seen in figure 6.7. This example uses the FEM/FMM hybrid method (see section 4.7) for calculating the potential on the surface of a cube with 68,921 vertices. The parameters are a MAC of $\theta = 0.5$ and a maximum multipole order of $P = 3$. Figure 6.8 shows the strong-scaling performance of the code from tens of thousands to tens of millions of DOFs or one to 256 CPUs. The image shows a three-fold increase in solve time for field evaluation of the boundary problem when increasing problem size by a factor of a thousand [67] using MPI only parallelization (i.e., no OpenMP) on the VSC3. The compute nodes provide two Intel Xeon E5-2650v2 2.6 GHz processors with eight cores each meaning that for a simulation on 256 CPUs 16 nodes are used. Simulations from 1 to 16 CPUs are done on a single node with MPI. Inter-node communication is done using infiniband.
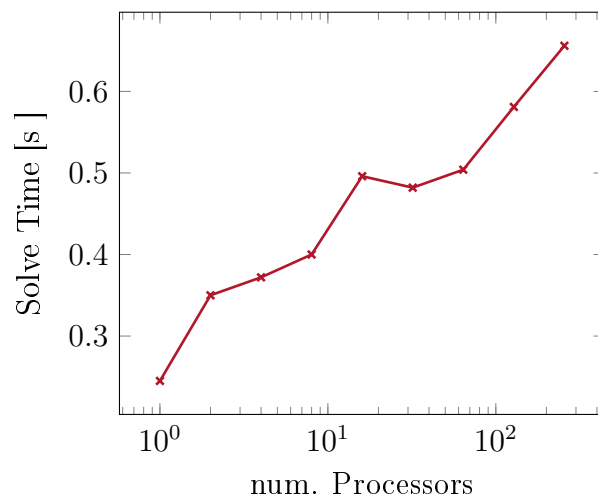
Figure 6.8.: This figure shows strong scaling from 6.9×10^4 to 7.06×10^7 vertices.

7. Conclusion

This work demonstrates the speed and feasibility of the Fast Multipole Method [FMM] for micromagnetism. All the necessary steps are derived, implemented, explained, and verified. The working implementation can be used for the stray-field calculation of the whole problem, in combination with existing finite element software, or as a Dirichlet boundary condition.

The software shows near optimal scaling on shared memory machines and the MPI implementation allows distributed execution of large meshes. The inherent scalability of the FMM, which focuses on minimizing inter-node communication, makes it an attractive solution for the foreseeable future where parallelization is the primary mode for increasing processing power.

The most time-consuming part of micromagnetism—the stray field—is successfully parallelized. That said, for a fully functional parallel micromagnetic code a parallel LLG time integration is still missing and would present an interesting follow-up project.

A. Appendix: Gaussian Quadrature

Gaussian quadrature is a method to approximate definite integrals over the region [-1;1] of a function $f(x)$ to a weighted sum:

$$\int_{-1}^{1} f(x)\,\mathrm{d}x = \sum_{i=0}^{n} w_i f(x_i) \tag{A.1}$$

with n evaluation points x_i and weights w_i. The approximation is exact for polynomials of degree $2n - 1$.

Gaussian quadrature can be extended to an integration over a triangle Δ with area A [76]:

$$\int_{\Delta} f(\mathbf{r})\,\mathrm{d}^2\mathbf{r} = A \sum_{i=1}^{N} w_i f(\mathbf{r}(\lambda_i)), \tag{A.2}$$

where λ are barycentric coordinates (see section 4.1). The weights and coordinates are tabulated in [76].

The function point $f(\mathbf{r}(\lambda))$ can easily be evaluated at evaluation point $\mathbf{r}(\lambda)$ by

$$\mathbf{r}(\lambda) = \sum_{j=0}^{3} \mathbf{r}_j \lambda_j, \tag{A.3}$$

where the index j indicates the vertex of the triangle Δ and should not be confused with the weight-index i.

Bibliography

[1] Dieter Suess, Thomas Schrefl, S. Fähler, Markus Kirschner, Gino Hrkac, Florian Dorfbauer, and Josef Fidler. Exchange spring media for perpendicular recording. *Applied Physics Letters*, 87(1):012504, 2005.

[2] Thomas Schrefl, Manfred E. Schabes, Dieter Suess, and Martin Stehno. Dynamic micromagnetic write head fields during magnetic recording in granular media. *IEEE transactions on magnetics*, 40(4):2341–2343, 2004.

[3] J.-E. Wegrowe and M.-C. Ciornei. Magnetization dynamics, gyromagnetic relation, and inertial effects. *American Journal of Physics*, 80(7):607–611, 2012.

[4] John O. Oti and Stephen E. Russek. Micromagnetic simulations of magnetoresistive behavior of sub-micrometer spin-valve MRAM devices. *IEEE Transactions on Magnetics*, 33(5):3298–3300, 1997.

[5] Said Tehrani, J. M. Slaughter, E. Chen, M. Durlam, J. Shi, and M. DeHerren. Progress and outlook for MRAM technology. *IEEE Transactions on Magnetics*, 35(5):2814–2819, 1999.

[6] Stuart SP Parkin, Masamitsu Hayashi, and Luc Thomas. Magnetic domain-wall racetrack memory. *Science*, 320(5873):190–194, 2008.

[7] Josef Fidler, Thomas Schrefl, Sabine Hoefinger, and Maciej Hajduga. Recent developments in hard magnetic bulk materials. *Journal of Physics: Condensed Matter*, 16(5):S455, 2004.

[8] Joachim Stöhr and Hans Christoph Siegmann. *Magnetism: From Fundamentals to Nanoscale Dynamics.* Springer Science & Business Media, January 2007. ISBN 978-3-540-30283-4. Google-Books-ID: XJjU2oQAbK0C.

[9] Helmut Kronmüller and Manfred Fähnle. *Micromagnetism and the Microstructure of Ferromagnetic Solids.* Cambridge University Press, August 2003. ISBN 978-0-521-33135-7. Google-Books-ID: h6nKtwcYyNEC.

[10] Alex Hubert and Rudolf Schäfer. *Magnetic Domains: The Analysis of Magnetic Microstructures.* Springer Science & Business Media, October 2008. ISBN 978-3-540-85054-0. Google-Books-ID: uRtqCQAAQBAJ.

[11] Richard Becker and Werner Döring. *Ferromagnetismus.* Springer-Verlag, 2013.

[12] Florian Bruckner, Christoph Vogler, Bernhard Bergmair, Thomas Huber, Markus Fuger, Dieter Suess, Michael Feischl, Thomas Fuehrer, Marcus Page, and Dirk Praetorius. Combining micromagnetism and magnetostatic Maxwell equations for multiscale magnetic simulations. *Journal of Magnetism and Magnetic Materials*, 343:163–168, October 2013. ISSN 0304-8853. doi: 10.1016/j.jmmm.2013.04.085. URL `http://www.sciencedirect.com/science/article/pii/S0304885313003156`.

[13] Florian Bruckner, Christoph Vogler, Michael Feischl, Dirk Praetorius, Bernhard Bergmair, Thomas Huber, Markus Fuger, and Dieter Suess. 3d FEM–BEM-coupling method to solve magnetostatic Maxwell equations. *Journal of Magnetism and Magnetic Materials*, 324(10):1862–1866, May 2012. ISSN 0304-8853. doi: 10.1016/j.jmmm.2012.01.016. URL `http://www.sciencedirect.com/science/article/pii/S0304885312000364`.

[14] K. Foster and M. F. Littmann. Factors affecting core losses in oriented electrical steels at moderate inductions. *Journal of Applied Physics*, 57(8):4203–4208, 1985.

[15] I. Sato. Further improvement of core loss in amorphous alloys. *Journal of Materials Engineering and Performance*, 2(2):235–239, 1993.

102

[16] Ryusuke Hasegawa. Amorphous magnetic materials—a history. *Journal of Magnetism and Magnetic Materials*, 100(1-3):1–12, 1991.

[17] F. E. Luborsky. Amorphous ferromagnets. *Handbook of Ferromagnetic Materials*, 1:451–529, 1980.

[18] Richard Boll. Soft magnetic metals and alloys. *Materials Science and Technology*, 1993.

[19] Ralph Skomski and J. M. D. Coey. *Permanent magnetism.* Institute of Physics Pub., 1999.

[20] J. Clerk Maxwell. A dynamical theory of the electromagnetic field. *Philosophical transactions of the Royal Society of London*, 155:459–512, 1865.

[21] Alberto P. Guimarães. Magnetic Domains. In *Principles of Nanomagnetism*. Springer, Cham, 2017. ISBN 978-3-319-59408-8 978-3-319-59409-5. doi: 10.1007/978-3-319-59409-5_2. URL `https://link.springer.com/chapter/10.1007/978-3-319-59409-5_2`.

[22] Pierre Weiss. L'hypothèse du champ moléculaire et la propriété ferromagnétique. *J. phys. theor. appl.*, 6(1):661–690, 1907. URL `https://hal.archives-ouvertes.fr/jpa-00241247/document`.

[23] Lale Landau and Evgeny Lifshitz. On the theory of the dispersion of magnetic permeability in ferromagnetic bodies. *Phys. Zeitsch. der Sowjetunion*, 8(153):101–114, 1935. URL `https://pdfs.semanticscholar.org/0c90/4c5ff5fff97bced606a5dc4d98cf9ebc4ed6.pdf`.

[24] William Fuller Brown Jr. Criterion for uniform micromagnetization. *Physical Review*, 105(5):1479, 1957. URL `https://journals.aps.org/pr/abstract/10.1103/PhysRev.105.1479`.

[25] John David Jackson. *Classical electrodynamics.* John Wiley & Sons, 2007.

[26] Werner Heisenberg. Multi-body problem and resonance in quantum mechanics II. *Z. f. Phys.*, 41:239, 1927.

[27] Paul Adrien Maurice Dirac. On the theory of quantum mechanics. In *Proceedings of the Royal Society of London A: Mathematical, Physical and Engineering Sciences*, volume 112, pages 661–677. The Royal Society, 1926.

[28] Tôru Moriya. Anisotropic superexchange interaction and weak ferromagnetism. *Physical Review*, 120(1):91, 1960.

[29] I. Dzyaloshinsky. A thermodynamic theory of "weak" ferromagnetism of antiferromagnetics. *Journal of Physics and Chemistry of Solids*, 4(4):241–255, 1958.

[30] Richard Phillips Feynman, Robert B. Leighton, and Matthew Sands. *The Feynman lectures on physics, vol. 2: Mainly electromagnetism and matter.* Addison-Wesley, 1979.

[31] Ivan Cimrák. A survey on the numerics and computations for the Landau-Lifshitz equation of micromagnetism. *Archives of Computational Methods in Engineering*, 15(3):1–37, 2007.

[32] Abert, Claas W. *Discrete Mathematical Concepts in Micromagnetic Computations, Dissertation.* PhD thesis, Uni Hamburg, Hamburg, 2013.

[33] Thomas L. Gilbert. A phenomenological theory of damping in ferromagnetic materials. *IEEE Transactions on Magnetics*, 40(6):3443–3449, 2004.

[34] T. L. Gilbert. A Lagrangian formulation of the gyromagnetic equation of the magnetization field. *Phys. Rev.*, 100:1243, 1955.

[35] P. Podio-Guidugli. On dissipation mechanisms in micromagnetics. *The European Physical Journal B - Condensed Matter and Complex Systems*, 19(3):417–424, February 2001. ISSN 1434-6028, 1434-6036. doi: 10.1007/s100510170318. URL `https://link.springer.com/article/10.1007/s100510170318`.

[36] Massimiliano d'Aquino, Claudio Serpico, and Giovanni Miano. Geometrical integration of Landau–Lifshitz–Gilbert equation based on the mid-point rule. *Journal of Computational Physics*, 209(2):730–753, 2005.

[37] Ernst Feldtkeller. Mikromagnetisch stetige und unstetige Magnetisierungskonfigurationen. *Zeitschrift für angewandte Physik*, 19(6), 1965. URL `https://scholar.google.com/scholar_lookup?hl=en&publication_year=1965&pages=530&issn=0044-2283&author=R.++Feldtkeller`.

[38] W. Döring. Point Singularities in Micromagnetism. *Journal of Applied Physics*, 39(2):1006–1007, February 1968. ISSN 0021-8979. doi: 10.1063/1.1656144. URL `http://aip.scitation.org/doi/10.1063/1.1656144`.

[39] André Thiaville, José Miguel García, Jacques Miltat, and Thomas Schrefl. Micromagnetic study of Bloch-point-mediated vortex core reversal. *Physical Review B*, 67(9):094410, 2003.

[40] Charles Kittel. *Introduction to solid state physics*. Wiley, 2005.

[41] Andreas Lyberatos, Dmitry V. Berkov, and Roy W. Chantrell. A method for the numerical simulation of the thermal magnetization fluctuations in micromagnetics. *Journal of Physics: Condensed Matter*, 5(47):8911, 1993.

[42] Stuart Parkin, Xin Jiang, Christian Kaiser, Alex Panchula, Kevin Roche, and Mahesh Samant. Magnetically engineered spintronic sensors and memory. *Proceedings of the IEEE*, 91(5):661–680, 2003.

[43] M. N. Baibich, J. M. Broto, A. Fert, F. Nguyen Van Dau, F. Petroff, P. Etienne, G. Creuzet, A. Friederich, and J. Chazelas. Giant Magnetoresistance of (001)Fe/(001)Cr Magnetic Superlattices. *Physical Review Letters*, 61(21):2472–2475, November 1988. doi: 10.1103/PhysRevLett.61.2472. URL `https://link.aps.org/doi/10.1103/PhysRevLett.61.2472`.

[44] S. Zhang and Z. Li. Roles of nonequilibrium conduction electrons on the magnetization dynamics of ferromagnets. *Physical Review Letters*, 93(12):127204, 2004.

[45] S. S. P. Parkin and D. Mauri. Spin engineering: Direct determination of the Ruderman-Kittel-Kasuya-Yosida far-field range function in ruthenium. *Physical Review B*, 44(13):7131, 1991.

[46] Ivan A. Sergienko and E. Dagotto. Role of the Dzyaloshinskii-Moriya interaction in multiferroic perovskites. *Physical Review B*, 73(9):094434, 2006.

[47] M. Heide, G. Bihlmayer, and S. Blügel. Dzyaloshinskii-Moriya interaction accounting for the orientation of magnetic domains in ultrathin films: Fe/W (110). *Physical Review B*, 78(14):140403, 2008.

[48] L. Lopez-Diaz, D. Aurelio, L. Torres, E. Martinez, M. A. Hernandez-Lopez, J. Gomez, O. Alejos, M. Carpentieri, G. Finocchio, and G. Consolo. Micromagnetic simulations using graphics processing units. *Journal of Physics D: Applied Physics*, 45(32):323001, 2012.

[49] André Thiaville, Stanislas Rohart, Émilie Jué, Vincent Cros, and Albert Fert. Dynamics of Dzyaloshinskii domain walls in ultrathin magnetic films. *EPL (Europhysics Letters)*, 100(5):57002, 2012.

[50] Leslie Greengard and Vladimir Rokhlin. A fast algorithm for particle simulations. *Journal of Computational Physics*, 73(2):325–348, 1987. URL `http://www.sciencedirect.com/science/article/pii/0021999187901409`. 15.

[51] Barry A. Cipra. The best of the 20th century: Editors name top 10 algorithms. *SIAM news*, 33(4):1–2, 2000.

[52] H. H. Long, E. T. Ong, Z. J. Liu, and E. P. Li. Fast Fourier transform on multipoles for rapid calculation of magnetostatic fields. *Magnetics, IEEE Transactions on*, 42(2):295–300, 2006. URL `http://ieeexplore.ieee.org/xpls/abs_all.jsp?arnumber=1580697`. 19.

[53] Boris Livshitz, Amir Boag, H. Neal Bertram, and Vitaliy Lomakin. Nonuniform grid algorithm for fast calculation of magnetostatic interactions in micromagnetics. *Journal of Applied Physics*, 105(7):07D541, 2009. URL `http://scitation.aip.org/content/aip/journal/jap/105/7/10.1063/1.3076048`. 8.

[54] L. Exl, W. Auzinger, S. Bance, M. Gusenbauer, F. Reichel, and T. Schrefl. Fast stray field computation on tensor grids. *Journal of Computational Physics*, 231(7):2840–2850, April 2012. ISSN 00219991. doi: 10.1016/j.

jcp.2011.12.030. URL `http://linkinghub.elsevier.com/retrieve/pii/`
`S0021999111007510`. 10.

[55] Robert C. Kirby and Anders Logg. The finite element method. In *Automated Solution of Differential Equations by the Finite Element Method*, Lecture Notes in Computational Science and Engineering, pages 77–94. Springer, Berlin, Heidelberg, 2012. ISBN 978-3-642-23098-1 978-3-642-23099-8. doi: 10.1007/978-3-642-23099-8_2. URL `https://link.springer.com/`
`chapter/10.1007/978-3-642-23099-8_2`.

[56] Philippe G. Ciarlet. *Numerical analysis of the finite element method*, volume 59. Presses de l'Université de Montréal, 1976.

[57] R. D. Graglia. Static and dynamic potential integrals for linearly varying source distributions in two- and three-dimensional problems. *IEEE Transactions on Antennas and Propagation*, 35(6):662–669, June 1987. ISSN 0018-926X. doi: 10.1109/TAP.1987.1144160. 23.

[58] A. H. Stroud. *Approximate calculation of multiple integrals*. Prentice-Hall, Englewood Cliffs, NJ, 1971.

[59] Markus Rech. *Effiziente Nahfeldkubatur in der Galerkin-Randelementmethode*. PhD thesis, Rheinische Friedrich-Wilhelms-Universität Bonn, 2002. URL `http://wissrech.ins.uni-bonn.de/teaching/diplom/`
`diplom_rech.pdf`.

[60] Wolfgang Hackbusch. *Integralgleichungen: Theorie und Numerik*, volume 68. Springer-Verlag, 2013.

[61] Shmuel Agmon. Multiple layer potentials and the dirichlet problem for higher order elliptic equations in the plane I. *Communications on Pure and Applied Mathematics*, 10(2):179–239, January 1957. ISSN 1097-0312. doi: 10.1002/cpa.3160100202. URL `http://onlinelibrary.wiley.com/doi/10.`
`1002/cpa.3160100202/abstract`.

[62] F. T. Johnson. A general panel method for the analysis and design of arbitrary configurations in incompressible flows. *National Aeronautics and Space*

Adminstration, Scientific and Technical Information Office, 3079, May 1980. URL `https://ntrs.nasa.gov/search.jsp?R=19800015776`.

[63] M. Duffy. Quadrature Over a Pyramid or Cube of Integrands with a Singularity at a Vertex. *SIAM Journal on Numerical Analysis*, 19(6):1260–1262, December 1982. ISSN 0036-1429. doi: 10.1137/0719090. URL `http://epubs.siam.org/doi/abs/10.1137/0719090`.

[64] Pietro Palmesi, Lukas Exl, Florian Bruckner, Claas Abert, and Dieter Suess. Highly parallel demagnetization field calculation using the fast multipole method on tetrahedral meshes with continuous sources. *Journal of Magnetism and Magnetic Materials*, 442:409–416, 2017. URL `http://www.sciencedirect.com/science/article/pii/S0304885316310162`.

[65] Chris Ceka. fmmtl/TaylorExpansionNotes.pdf at master · ccecka/fmmtl, April 2015. URL `https://github.com/ccecka/fmmtl/blob/master/references/TaylorExpansionNotes.pdf`.

[66] Linbo Zhang, Tao Cui, Hui Liu, and others. A set of symmetric quadrature rules on triangles and tetrahedra. *Journal of Computational Mathematics*, 27(1):89–96, 2009. URL `https://www.researchgate.net/profile/Linbo_Zhang3/publication/228667586_A_set_of_symmetric_quadrature_rules_on_triangles_and_tetrahedra/links/00b7d530bfbd76b485000000.pdf`. 25.

[67] R. Yokota, D. Koyama, C.-H. Lai, and N. Yamamoto. An FMM based on dual tree traversal for many-core architectures. *Journal of Algorithms & Computational Technology*, 7(3):301–324, 2013. URL `http://multi-science.atypon.com/doi/abs/10.1260/1748-3018.7.3.301`. 18.

[68] Felipe A. Cruz and L. A. Barba. Characterization of the errors of the FMM in particle simulations. *International Journal for Numerical Methods in Engineering*, 79(13):1577–1604, September 2009. ISSN 00295981, 10970207. doi: 10.1002/nme.2611. URL `http://arxiv.org/abs/0809.1810`. arXiv: 0809.1810.

[69] G. Akoun and J. P. Yonnet. 3d analytical calculation of the forces exerted between two cuboidal magnets. *IEEE Transactions on Magnetics*, 20(5):1962–1964, September 1984. ISSN 0018-9464. doi: 10.1109/TMAG.1984.1063554.

[70] P. Palmesi, C. Abert, F. Bruckner, and D. Suess. Convergence of highly parallel stray field calculation using the fast multipole method on irregular meshes. *AIP Advances*, 8(5):056019, December 2017. doi: 10.1063/1.5006896. URL http://aip.scitation.org/doi/full/10.1063/1.5006896.

[71] R. D. McMichael, M. J. Donahue, D. G. Porter, and Jason Eicke. Switching dynamics and critical behavior of standard problem No. 4. *Journal of Applied Physics*, 89(11):7603–7605, June 2001. ISSN 0021-8979. doi: 10.1063/1. 1355356. URL http://aip.scitation.org/doi/abs/10.1063/1.1355356.

[72] Claas Abert, Lukas Exl, Florian Bruckner, André Drews, and Dieter Suess. magnum. fe: A micromagnetic finite-element simulation code based on FEniCS. *Journal of Magnetism and Magnetic Materials*, 345:29–35, 2013.

[73] Anders Logg and Garth N. Wells. DOLFIN: Automated Finite Element Computing. *ACM Trans. Math. Softw.*, 37(2):20:1–20:28, April 2010. ISSN 0098-3500. doi: 10.1145/1731022.1731030. URL http://doi.acm.org/10.1145/1731022.1731030.

[74] Dieter Suess, Vassilios Tsiantos, Thomas Schrefl, Josef Fidler, Werner Scholz, Hermann Forster, Rok Dittrich, and J. J. Miles. Time resolved micromagnetics using a preconditioned time integration method. *Journal of Magnetism and Magnetic Materials*, 248(2):298–311, 2002. URL http://www.sciencedirect.com/science/article/pii/S0304885302003414.

[75] Claas Abert, Lukas Exl, Gunnar Selke, André Drews, and Thomas Schrefl. Numerical methods for the stray-field calculation: A comparison of recently developed algorithms. *Journal of Magnetism and Magnetic Materials*, 326:176–185, January 2013. ISSN 0304-8853. doi: 10.1016/j.jmmm. 2012.08.041. URL http://www.sciencedirect.com/science/article/pii/S0304885312007299. 20.

[76] G. R. Cowper. Gaussian quadrature formulas for triangles. *International Journal for Numerical Methods in Engineering*, 7(3):405–408, January 1973. ISSN 1097-0207. doi: 10.1002/nme.1620070316. URL `http://onlinelibrary.wiley.com/doi/10.1002/nme.1620070316/full`.

Curriculum Vitae

Pietro PALMESI

PLACE AND DATE OF BIRTH:	Austria | 20 December 1985
ADDRESS:	Hintzerstr. 2/18, 1030 Vienna, Austria
PHONE:	+43 660 401 55 62
EMAIL:	pietro@palmesi.com

Education

OCT 2011 - JUL 2014	Master of Science
	Vienna University of Technology, Austria
Thesis:	"Thermal Description of GMR Sensors Using Monte-Carlo Simulations Based on the Stoner-Wohlfarth Model"
	| Advisor: Priv. Doz. Dr. Dieter SUESS
SEP 2006 - OCT 2011	Bachelor of Science
	Vienna University of Technology, Austria
	| Advisor: Dr. Stefan RADEL
SEP 2000 - JUN 2005	High School, **HTL Donaustadt**, Austria

_____   _____

(Date)   (Signature Dipl.-Ing. Pietro Palmesi)